Stochastic Environmental Research and Risk Assessment
https://doi.org/10.1007/s00477-025-03016-x

ORIGINAL PAPER

Application of wavelet transform for extracting and analysing evapotranspiration-induced diel fluctuations in streamflow records

M. Waqas Sarwar[1] · **Ali Shokri**[1]

Accepted: 10 May 2025

Abstract
Diurnal fluctuations in groundwater and streamflow are produced due to evapotranspiration, indicating a strong connection between streamflow and the groundwater reservoir. Studying the patterns of diel fluctuations can provide valuable information on the hydrological processes in a catchment. Analysing these fluctuations makes it possible to estimate the evapotranspiration rate as well. In this paper, the signal analysis technique of the wavelet transform is applied to the streamflow time series to extract and analyse diel fluctuations. The performance of two main types of wavelet transform, continuous and discrete, is assessed against widely applied methods of trend extraction, such as moving average. The results show that wavelet transform can be used successfully to identify periodic and non-periodic features of the time series, such as seasonal and trend components, and to distinguish between signal and noise. The continuous wavelet transform demonstrates that the diurnal component of streamflow exhibits significant variation over different temporal scales, with the dominant periods ranging from 12 to 36 h. In conclusion, the findings suggest that wavelet transform can effectively capture evapotranspiration-induced diurnal streamflow fluctuations and provide insights into the hydrological processes at different temporal scales.

Keywords Wavelet transform · Evapotranspiration · Time–frequency analysis

1 Introduction

Diurnal fluctuations in groundwater and streamflow are high-frequency oscillations produced due to the natural dynamic response of the groundwater reservoir against external environmental forces like evapotranspiration (ET). Studies of diel (referred to interchangeably with diurnal in this article) fluctuations in streamflow reveal the temporal patterns and dynamics of water movement and storage in streams, affecting the stream system's water quality, ecology, and management (Kirchner et al. 2020). In addition, diel fluctuations in groundwater and streamflow indicate a robust connection between them (Széles et al. 2018). When diel fluctuations in groundwater and streamflow are observed, it suggests a complex interaction and water exchange between the stream and the underlying groundwater system. Therefore, analysis of diel fluctuations can reveal key hydrological characteristics of a catchment, like the sources and pathways of water in streams (Barnard et al. 2010), the rates and magnitudes of water exchange between streams and their surrounding environments, and the impacts of human activities on stream hydrology (Satchithanantham et al. 2017).

Some studies have analysed diel fluctuations to estimate riparian ET by computing the streamflow loss during each diel cycle (White 1932; Troxell 1936; Tschinkel 1963; Boronina et al. 2005; Gribovszki et al. 2008; Loheide II 2008; Cadol et al. 2012; Sarwar et al. 2022). While some others have focused on investigating the origin and the mechanisms of propagation of the diel signals in Streamflow (Barnard et al. 2010; Graham et al. 2012).

In recent years, hydrologists have used time–frequency analysis methods to understand better the complex dynamics and characteristics of variations and trends in hydrological time series. For example, (Lundquist and Cayan 2002) showed the capabilities of applying time–frequency techniques like the Fourier Transform in identifying the distinct periods where diel signals predominately affect baseflow recession.

✉ M. Waqas Sarwar
ms511@students.waikato.ac.nz; waqasmlk93@gmail.com

[1] School of Engineering, University of Waikato, Hamilton 3216, New Zealand

Published online: 05 June 2025

Similarly, Wavelet analysis is another practical time–frequency approach utilised to examine variations, periodicities, and trends in diverse geophysical time series (Mallat 2009). Compared to Fourier analysis, Wavelet analysis offers the advantage of revealing different time–frequency components within a time series that can be localised in both the temporal and frequency domains (Smith et al. 1998).

Wavelet analysis has been applied in hydrology since the early 1990s due to its ability to analyse non-stationary datasets (Rhif et al. 2019; Sang 2013). It has been shown that Wavelet analysis is an effective tool for extracting non-trivial and potentially useful time–frequency information from non-stationary data sets available in geosciences (Percival 2008). Some of the applications of Wavelet analysis in hydrology are multiresolution analysis of hydrologic time series (Chong et al. 2019), denoising of hydrologic series to allow for the detection of underlying trends and variations (Sang 2012), simulation and forecasting of hydrologic series using wavelet-aided convolution neural networks (Adamowski and Sun 2010), and analysing groundwater level fluctuations including decomposition of time series into different frequency components (Huang et al. 2021). Moreover, derivative techniques of wavelet transform, like Wavelet cross-correlation and coherent analysis, are used by (Briciu et al. 2019) to compare and correlate upstream and downstream diurnal cycles of different water quality parameters.

Further, CWT can aid in characterising extreme events such as floods or droughts by revealing their temporal signatures and how they may change over time in relation to the macroclimate indexes (Santos and de Morais 2013). Studies by (Sang 2013; Zhang et al. 2015) have used the time–frequency information from CWT to improve forecast models' accuracy and hydrological processes' accuracy. Combining CWT with statistical models like ARIMA improved forecasting models for hydrological time series by capturing the non-stationary characteristics of hydrological time series (Wu et al. 2021). CWT has models. Additionally, wavelet analysis methods have been used to study the characteristics of hydrological processes and their applications, including serial correlation analysis, frequency analysis, and fuzzy analysis (Sang 2013).

Understanding the daily characteristics of streamflow offers a window into the time-varying impact of different environmental parameters on catchment hydrological processes. However, investigating diel fluctuations presents challenges due to the intricate and highly variable spatio-temporal nature of the hydrological dynamics involved in these processes (Graham et al. 2012). The numerical and analytical methods utilised in the abovementioned studies have been valuable for quantifying the link between diel signals and ET. However, these methods do not fully capture the entire range of information on diurnal characteristics. They fall short of capturing details such as the timing and magnitude of the daily peaks, which can vary across different periods and locations (Xiao et al. 2018). This limitation comes from the fact that these methods primarily focus on the time domain of streamflow signals, neglecting the frequency components of the streamflow signal (Yan et al. 2020). Diurnal fluctuations are naturally occurring frequency-based phenomena, and only relying on time-domain analyses could lead to the oversight of crucial frequency-dependent patterns and dynamics (Grinsted et al. 2004; Rhif et al. 2019).

However, the previous studies examining diurnal fluctuations in streamflow have primarily relied on time-domain analyses, such as calculating mean daily streamflow values or investigating trends in the data (Czikowsky and Fitzjarrald 2004; Loheide II 2008; Sarwar et al. 2022). While these methods provide valuable insights into the overall daily hydrological behaviour of the system, they may not fully capture the comprehensive range of information on daily characteristics. These approaches often overlook critical frequency-dependent patterns and dynamics inherent in diurnal fluctuations, which can be essential for understanding the temporal impact of environmental parameters on catchment hydrological processes (Percival 2008).

This study addresses these limitations by employing Wavelet analysis to investigate the temporal changes in diurnal streamflow fluctuations. The specific objectives of this study are: (1) to choose the optimal wavelet family to decompose streamflow time series into multiple lower resolution levels, (2) to remove trends using wavelet thresholds and extract diel signals, and (3) to represent diel signals at different scales and times through a power spectrum of the continuous wavelet transform.

2 Methodology

2.1 Overview of continuous and discrete wavelet transform

Wavelet analysis has two main types: continuous wavelet transform (CWT) and discrete wavelet transform (DWT) (Vetterli and Herley 1992). The following integrated expression gives the CWT of a signal $x(t)$

$$\tilde{x}(\tau, s) = \frac{1}{\sqrt{s}} \int_{-\infty}^{+\infty} x(t) * \overline{\psi}_{s,\tau}(t)\, dt \tag{1}$$

where $\tilde{x}(\tau, s)$ is the transformed signal, τ is the translation parameter, which controls the locations of the wavelet, s is the scaling parameter, which controls the width of the

wavelet, and $\psi_{s,\tau}(t)$ refers to a wavelet basis function at that particular scale and translation of the mother wavelet $\psi(t)$. A mother wavelet with different scaling and translation factors can generate countless daughter wavelets.

$$\psi_{s,\tau} = \frac{1}{\sqrt{s}}\psi\left(\frac{t-\tau}{s}\right) \tag{2}$$

As an illustration, Fig. 1 presents a schematic demonstrating how CWT effectively captures both the low and high-frequency components of the signal. The mother wavelet $\psi(t)$ undergoes continuous scaling (τ) and translation (s) operations, spanning the entire signal length multiple times. With each pass of CWT, a distinct daughter wavelet (for example $\psi_{s1,\tau1}(t)$ and $\psi_{s2,\tau2}(t)$) convolves with the signal, generating an array of coefficients that represent the degree of similarity between the signal and the wavelet at that particular scale and position. This process enables the identification and localisation of signal features with varying frequencies, making CWT a powerful tool for time–frequency analysis. The resulting CWT coefficients provide valuable insights into the signal's time-varying characteristics and underlying dynamics, enhancing our understanding of complex time series data (Mallat 2009; Debnath and Shah 2017).

The decomposed arrays of CWT coefficients represent their different constituent frequency components, while their magnitude indicates the presence of specific frequencies at different time points. Therefore, CWT coefficients provide valuable insights into the signal's time-varying characteristics and underlying dynamics, enhancing our understanding of complex time series data (Mallat 2009; Debnath and Shah 2017).

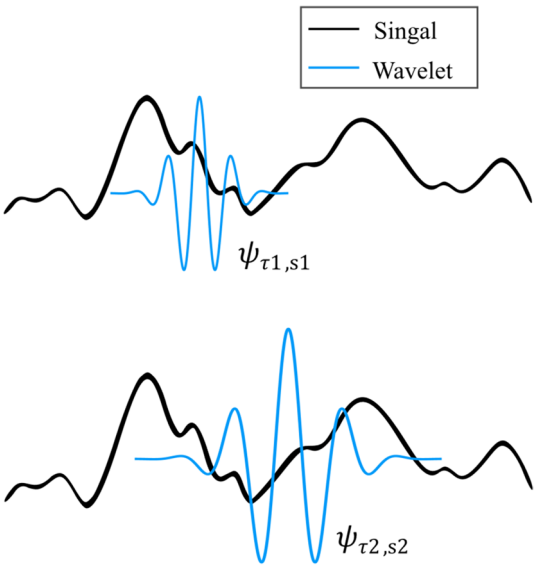

Fig. 1 Continuous Wavelet Transform (CWT) Principle: Illustrating the CWT process involving the convolution of the Morlet wavelet with the signal at various scales and translations. This enables the extraction of both low and high-frequency components. In this depiction, $\psi_{s1,\tau1}(t)$ denotes a contracted form of the mother wavelet, while $\psi_{s2,\tau2}(t)$ corresponds to a scaled version

Many types of mother wavelets are found in the literature, each with unique advantages and applications (Misiti 2007). For example, the Morlet wavelet utilised in this study can effectively analyse oscillatory patterns in time-series data, proving invaluable in signal processing and neuroscience, where detecting transient events and rhythmic patterns is crucial.

The CWT of a signal involves significant overlapping of wavelets at and between different scales, which results in redundant information, i.e., duplicate arrays of coefficients. The redundancy might provide high resolution but requires substantial computational resources (Addison 2018). One solution to this problem is to use the DWT method, where the scale and translation parameters are restricted to discrete values that are $s = a_0^m$ and $\tau = nb_0a_0^m$ ($a_0, b_0 \in R+$; $m, n \in Z$), respectively. The integer m is the resolution level of DWT, and n is the proportionality constant (Mallat 2009).

Implementing discrete scale and translation parameters in Eq. 2 yields:

$$\psi_{m,n}(t) = \frac{1}{\sqrt{a_0^m}}\psi\left(\frac{t-nb_0a_0^m}{a_0^m}\right) \tag{3}$$

For convenience, DWT is operated as low and high pass filters on a dyadic grid ($a_0=2$) with a fixed-width wavelet ($b_0=1$). The wavelet function $\psi(t)$ and a related scaling function, $\varphi(t)$ are defined as

$$\psi_{m,n}(t) = g_k\sqrt{2^m}\psi(2^m t - n) \tag{4}$$

$$\varphi_{m,n}(t) = h_k\sqrt{2^m}\psi(2^m t - n) \tag{5}$$

where g_k and h_k are low- and high-pass filters, respectively.

DWT provides a much more concise set of information as compared to CWT. During each DWT pass, the signal is divided into several coefficient arrays called detailed and approximation coefficients. The division is based on a cut-off frequency fs, which is often the most dominant frequency in the signal. The detail coefficient cD_n captures all the high-frequency components (noise) at level n, while the approximation coefficient comprises all the remaining high-frequency components (noise + trend). In each successive pass, the DWT is applied on the approximation coefficient cA_n further divide it into sub-signals cD_{n+1} and cA_{n+1}. The iterative process of signal decomposition continues until either the desired level of decomposition is achieved, or the signal length can no longer be halved. The pyramid-like discretisation makes DWT a more straightforward analysis than CWT (Mallat 2009; Percival 2008). This also enables

a more accurate signal reconstruction from a given set of DWT coefficients. Based on these advantages, this study uses DWT to decompose diel streamflow signals into their temporal components to identify trends and reconstruct detrended signals.

2.2 Application of DWT for trend removal with wavelet thresholding

Wavelet thresholding is utilised for distinguishing noise, including diurnal oscillations, from the streamflow recession signal in detecting diurnal oscillations. The fundamental concept behind wavelet thresholding is eliminating noise components that do not meet the specified thresholding criteria from the detail components. This process produces a reconstructed signal representing the original signal's non-oscillatory trend. By utilising threshold-based wavelength detrending, sudden spikes and drops in the signal can be smoothed out, allowing for the extraction of time–frequency information associated with the non-oscillatory fluctuations. This helps to reveal and emphasise the underlying patterns or trends in the data while effectively isolating the diurnal oscillations from other noise sources.

In wavelet thresholding, the signal is first decomposed into its "dyadic components" and then reconstructed by applying a specific thresholding value denoted as λ. The denoising through wavelet thresholding involves determining appropriate thresholds for each level of the time scale, typically done using a specific method. These determined thresholds are then applied with a suitable thresholding rule to effectively remove unwanted noise from the primary signal. By using this approach, wavelet thresholding can efficiently reduce noise while preserving the essential features of the original signal.

2.2.1 Threshold calculation

A threshold scheme depending on the decomposition level (Johnstone and Silverman 1997) is employed where a unique λ_i is calculated for each detailed component based on its noise strength σ_i, and applied to each decomposition level individually.

$$\lambda_i = \sigma_i \sqrt{2.ln\left(N_i\right)} \tag{6}$$

where σ is the noise strength, and N_i is the length of detailed coefficients at each resolution level i. The noise strength at each level is calculated as

$$\sigma_i = \frac{1}{0.6745} \sum_{t=1}^{N_i} \left|cD_i\left(t\right)\right| \tag{7}$$

The signal is then reconstructed using the list of thresholded detail coefficients. Noise is removed from all the detailed coefficients at each level. The resulting signal represents the underlying trend.

2.2.2 Thresholding rules

A threshold rule is a criterion that filters out detailed coefficients using a thresholding value λ. There are three main types of thresholding rules.

In soft thresholding, the wavelet coefficients with significant positive and negative magnitudes above λ are shrunk toward zero. The soft thresholding is given as

$$cD_i'\left(t\right) = \begin{cases} sgn\left(cD_i\left(t\right)\right).\left(\left|cD_i\left(t\right)\right| - \lambda\right) \left|cD_i\left(t\right)\right| > \lambda \\ 0 \left|cD_i\left(t\right)\right| \le \lambda \end{cases} \tag{8}$$

where $cD\prime_i\left(t\right)$ is the modified detail coefficient and *sgn(x)* is the sign function

$$\mathrm{sgn}\left(x\right) = \begin{cases} 1x > 0 \\ 0x = 0 \\ -1x < 0 \end{cases} \tag{9}$$

The second thresholding rule is hard thresholding. In hard thresholding, detail coefficients whose value falls below λ are discarded immediately (Andrecut, 2019). The hard thresholding is given as

$$cD_i'\left(t\right) = \begin{cases} cD_i\left(t\right) \left|cD_i\left(t\right)\right| > \lambda \\ 0 \left|cD_i\left(t\right)\right| \le \lambda \end{cases} \tag{10}$$

The third type of traditional thresholding rule is the non-negative garrotte thresholding.

$$cD_i'\left(t\right) = \begin{cases} cD_i\left(t\right) - \frac{\lambda^2}{cD_i\left(t\right)} \left|cD_i\left(t\right)\right| > \lambda \\ 0 \left|cD_i\left(t\right)\right| \le \lambda \end{cases} \tag{11}$$

It is intermediate between hard and soft thresholding and provides a compromise between the two. It behaves like soft thresholding for values significantly above the threshold and reflects the properties of hard thresholding for low input values (Gao 1998). All three thresholding rules are applied in the analysis to the entire set of discrete wavelet families. Figure 2 visually represents how the three thresholds compare using a sample array of wavelet coefficients. The thresholding is applied between − 0.5 and 0.5. The thresholding rules differ in treating the input coefficients outside the specified noise range. In soft thresholding, the non-noise coefficients are shrunk to zero on either noise threshold. On the other hand, no scaling is performed in hard thresholding, and all the non-noise coefficients are kept unchanged. The

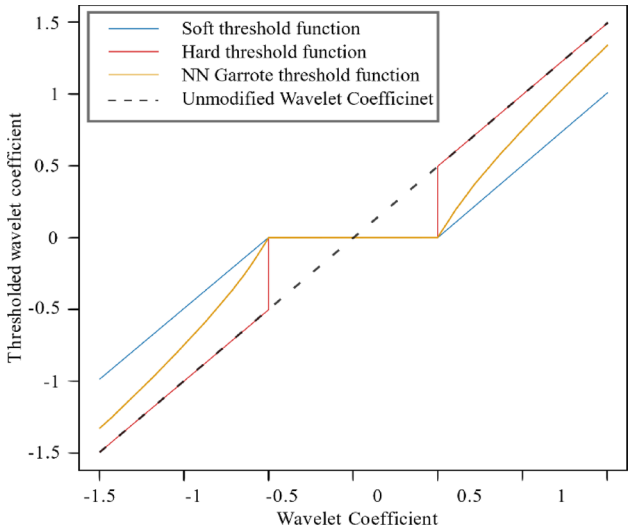

Fig. 2 Comparative Visualization of Soft, Hard, and Garrotte Thresholding Rules: The X-axis shows the input values, while the Y-axis displays the corresponding thresholded output values

Garrotte thresholding provides a compromise between soft and hard thresholding. The coefficients gradually shrunk between zero and the original values as we moved from smaller to larger coefficients. The garrotte offers advantages over hard and soft shrinkage, including smaller mean-square error and less sensitivity to small perturbations in the data (Fourati et al. 2005).

2.2.3 Wavelet selection

One of the key advantages of a Wavelet analysis is the availability of different wavelet basis functions called mother wavelets, which can be used for various types of analysis (Daubechies 1988; Mallat 2009; Zeshang Yang et al. 1995). However, the output of wavelet analysis is highly dependent on the mother wavelet used, and care should be taken when choosing the appropriate wavelet. For this study, we tested 106 different Wavelet basis functions available in the Python library.

2.2.3.1 Performance indices The main criteria for selecting an optimal Wavelet are the signal-to-noise ratio (SNR) and the similarity of the denoised signal with a reference diurnal waveform. The SNR is calculated for each denoised signal. It serves as a crucial metric to quantify the amount of the desired signal against the noise present in the signal. A higher SNR indicates that the denoised signal has less noise and more of the desired signal. The SNR is expressed as

$$SNR = 10ln\frac{\sum y^2}{\sum \sqrt{y-\tilde{y}}^2} \tag{12}$$

where y is the original signal and $\tilde{y}$ is the denoised signal. A higher SNR value indicates a better denoising performance.

Along with SNR, quantitative indices like root mean square error (RMSE) and correlation coefficient are calculated to identify the similarity between the denoised signal and a reference diurnal signal. A lower RMSE indicates a closer match to the reference signal. RMSE is given by:

$$RMSE = \sqrt{\frac{\sum (y-\tilde{y})^2}{length\,(y)}} \tag{13}$$

The wavelet function that produces a detrended signal with the lowest SNR and RMSE values is considered optimal.

2.2.3.2 Selection process The selection process is shown in the flowchart in Fig. 3.

- Firstly, an appropriate wavelet function is selected from the family of discrete wavelets, and the signal is detrended with wavelet detrending under all three thresholding rules.
- Following the detrending, the spectral density of the denoised signals is analysed using the Fast Fourier Transform (FFT) algorithm to find the dominant frequency in the signal. The resulting FFT information is used to filter out wavelets where the dominant frequency of the denoised signal significantly differed from a diurnal frequency, i.e., 24 h.
- In cases where the dominant frequency is not diurnal (24-h cycle), the detrended signal is deemed unfit and discarded, and the wavelet detrending process is repeated with another wavelet function.
- Conversely, if the signal corresponds to a diurnal attribute, it is retained for further calculations, which include the calculation of SNR, RMSE, and R^2 against the reference denoised signal.
- Finally, an optimal wavelet function with the lowest SNR and RMSE values is selected, which ensures the wavelet's denoising ability while minimising noise interference.

2.3 Automating extraction of diurnal signals using continuous wavelet transform

2.3.1 Modification of DWT process

The detrending process from discrete wavelet transform has been shown to effectively remove noise from hydrological series and reveal the time–frequency employed to minimise these effects, but sometimes doing so produces undesirable

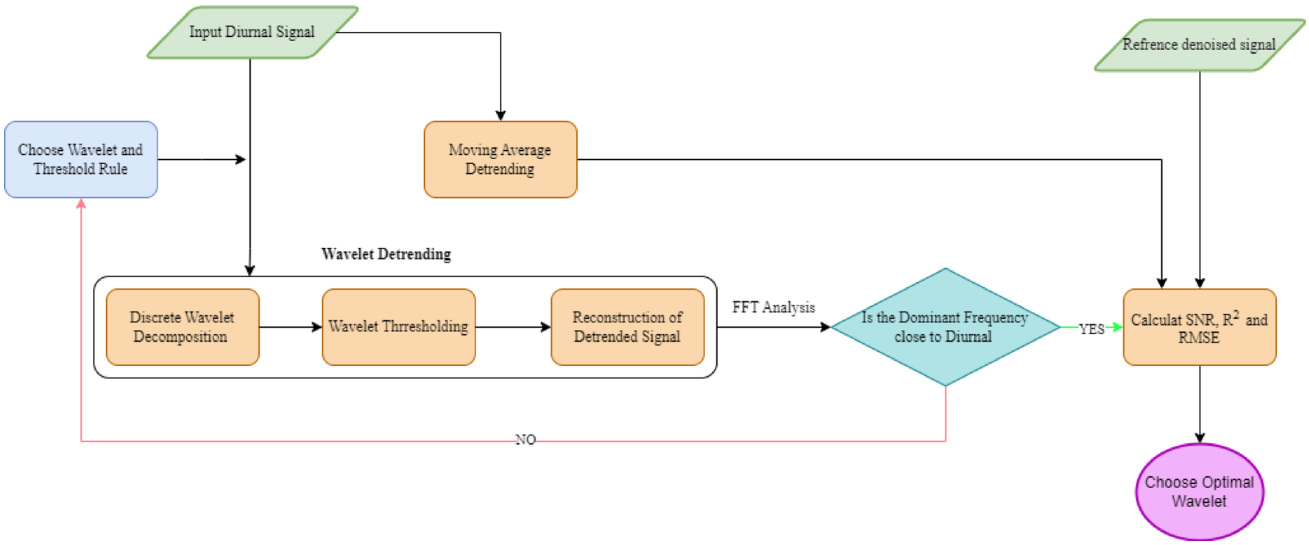

Fig. 3 Flow chart for the selection of appropriate wavelet for optimal extraction of diel signals from synthetic sample fluctuating signals and observed streamflow

artifacts into the decomposition and makes it difficult to accurately detrend lengthy data, primarily when the trend extends near the boundaries (Lukas et al. 2016; Mallat 2009) However, DWT has some limitations when applied to detrend a long-term signal: (1) DWT introduces boundary effects at the edges of a times series. (2) The wavelet basis functions have limited support in time, which means they are not well-suited for modeling long-term trends (Mallat 2009). To address these issues and make DWT work with our long-term streamflow data, the entire length of the time series is divided into overlapping sections of a finite length. The DWT coefficients are calculated on overlapping sections, and the detrended part of the section is obtained. The final detrended signal is obtained by stitching together all the individual detrend sections. The average is calculated at the central point. The detrending process removes the more significant frequency components associated with the trend and prepares the data nicely for a more accurate application of the continuous wavelet transform.

2.3.2 Extraction of diurnal episodes

The steps involved in the CWT extraction process are as follows:

1. The frequency range corresponding to the diel signals of interest is defined to capture the variations appropriately. Regarding diurnal fluctuations, the coefficient arrays for frequencies between 23 and 25 h are chosen for further analysis.
2. Timestamps are identified where the magnitudes of the selected diel coefficients are the largest compared to the neighbouring noise or non-diel components.
3. These timestamps are then used to extract episodes of diurnal fluctuations from the detrended dataset.
4. Refinements are made to the extracted episodes, like removing Streamflow records exhibiting significant power spectrum distortion due to precipitation from the analysis.
5. Diurnal episodes lasting less than four days are discarded from the analysis as employed in similar studies (Sarwar et al. 2022) as an optimal minimum length to identify visible trends in the episode.
6. Diurnal episodes with peaks falling outside of the 5th–95th quantiles are removed as they are associated with precipitation events and have a high noise component attribution.
7. Episodes occurring during the Autumn and Winter months (April–May–June–July) are also discarded, as the diurnal fluctuations in those months cannot be associated with ET due to frequent precipitation and decreased temperatures.

The whole process is automated through a Python script, enabling swift extraction of diurnal signals from extensive streamflow data.

3 Testing of proposed methods

The proposed method is tested on two distinct datasets: a synthetic signal (SS) and a real-world streamflow (RS) dataset. The synthetic dataset provides an ideal, controlled scenario where the true noise characteristics are known. The methodology is assessed and validated under controlled conditions before its application to real data. No direct

parameter optimisation is performed using synthetic data; instead, the same methodological framework is applied to both datasets. Moreover, wavelet selection and denoising performance are evaluated independently for each dataset to account for their inherent differences (Fig. 4).

For SS, the reference signal consists of artificially introduced oscillatory noise designed to mimic diurnal fluctuations. This allows for a direct comparison between the noise components extracted by the proposed method and those intentionally added, providing a clear validation of its accuracy. In contrast, for RS, a lagged ET signal is used as a reference because diurnal fluctuations in streamflow are closely related to ET or PET through a specific lag time (Sarwar et al. 2022).

Additionally, for both datasets, the performance of the proposed method is benchmarked against traditional detrending techniques, such as the rolling mean, which has been widely adopted for its simplicity in prior studies to isolate diurnal fluctuations (Boronina et al. 2005; Gribovszki et al. 2008; Kirchner et al. 2020).

3.1 Hypothetical scenario

The SS is generated based on the suggestion provided by Kirchner et al. (2020), which represents diel fluctuations in the streamflow recession.

$$y = b^{-at} + sin\left(2\pi vt\right) * c^{-at} + noise \tag{14}$$

where a is the recession constant, b is initial streamflow, c is the diel amplitude, and noise is a signal having a standard normal distribution with an average of 0 and a standard deviation of 1 (also known as Gaussian white noise). The noise function with $\mu = 0$ and $\sigma = 1$ is

$$p\left(x\right) = \frac{1}{\sqrt{2\pi}} e^{\frac{-x^2}{2}} \tag{15}$$

3.2 Real streamflow scenario

Hourly streamflow data from the Toenepi stream in Waikato, New Zealand, is applied to investigate the application of WT on Streamflow daily fluctuations (Fig. 5). The Toenepi stream (WGS84 coordinates: − 37.7146, 175.5632) drains a small catchment in the Waikato region, New Zealand. The catchment has an area of 1.6 ha, and an elevation range from 40 to 130 m above mean sea level. The sub-catchment is a headwater catchment, with a flat (max slope 6.5%) and fully covered by pasture apart from the riparian plantings around the Toenepi stream, mainly consisting of shading trees and shrubs (Wilcock et al. 2009). There is adequate vegetation along the stream route and a moderately well-drained aquifer. The catchment showed daily fluctuations in the streamflow recessions, particularly in warmer months (Sarwar et al. 2022).

The process is first applied to a single summer recession to compare the detrending performance of methods like DWT and moving average (Fig. 6). The recession is selected to represent the typical characteristics and fluctuation patterns

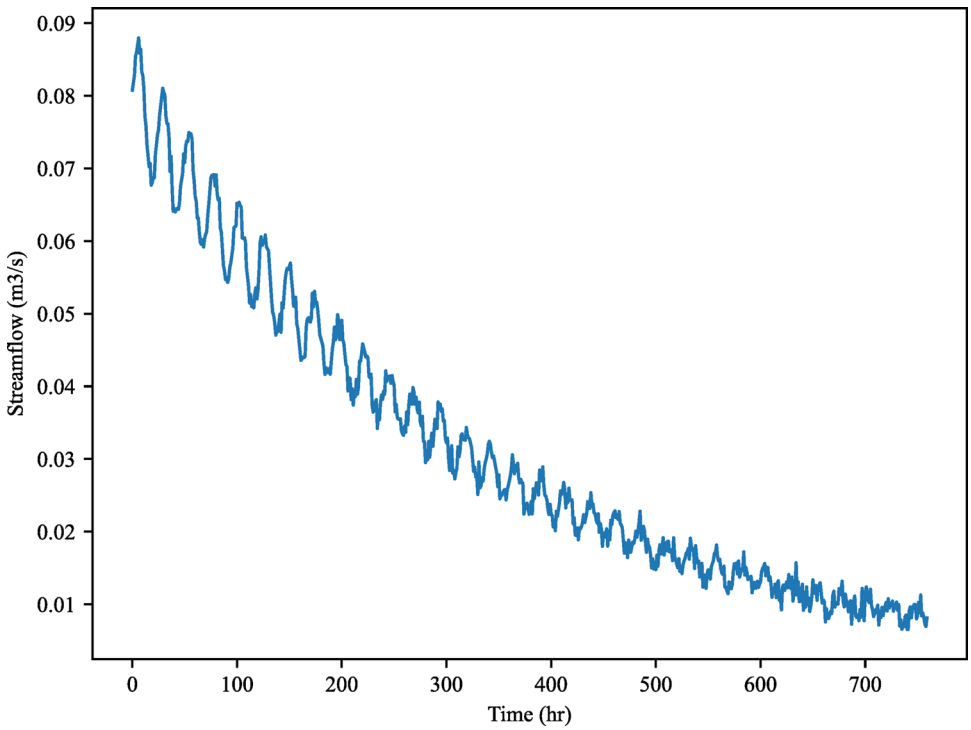

Fig. 4 Synthetic flood recession with daily fluctuations when a = 0.003, b = 0.08, and c = 0.008

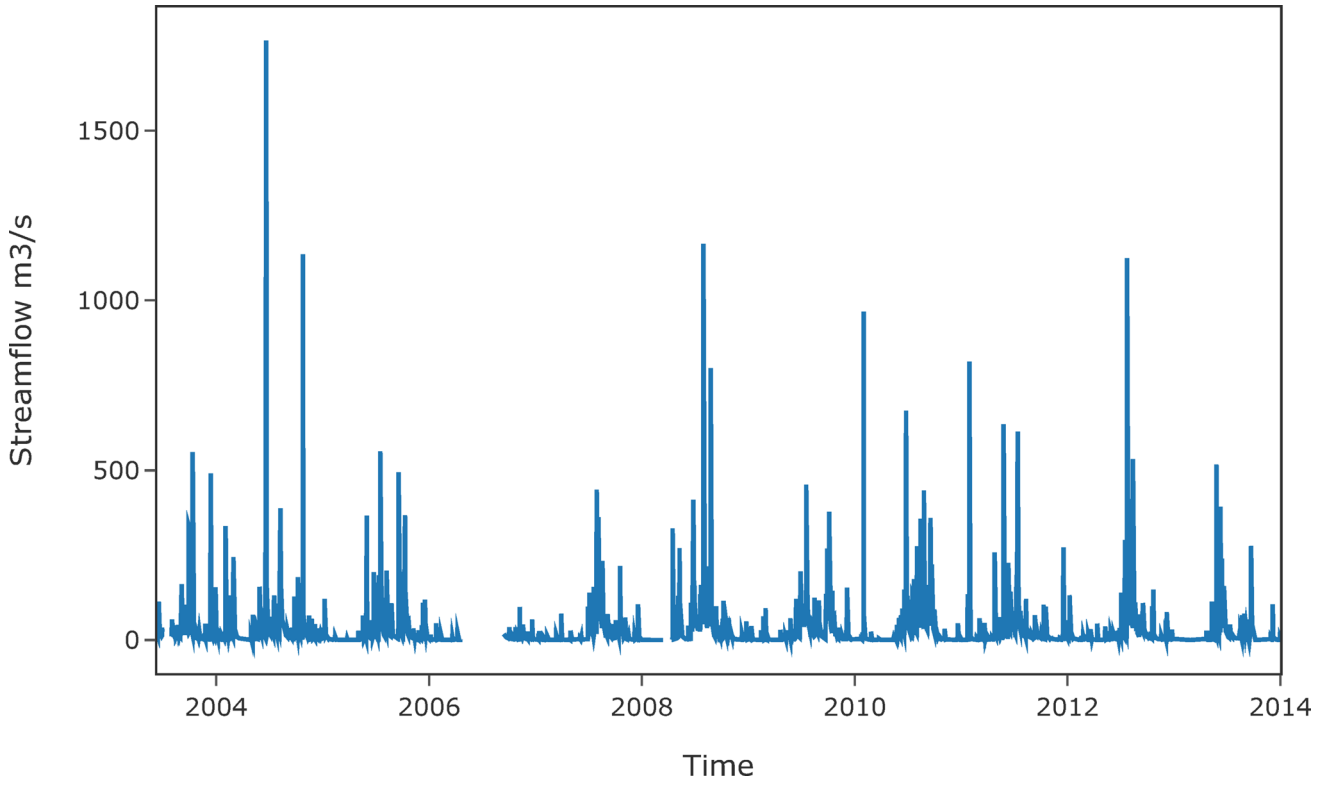

Fig. 5 Hourly streamflow series for Toenepi, Waikato

Fig. 6 Streamflow signal from Toenepi showing diurnal fluctuations

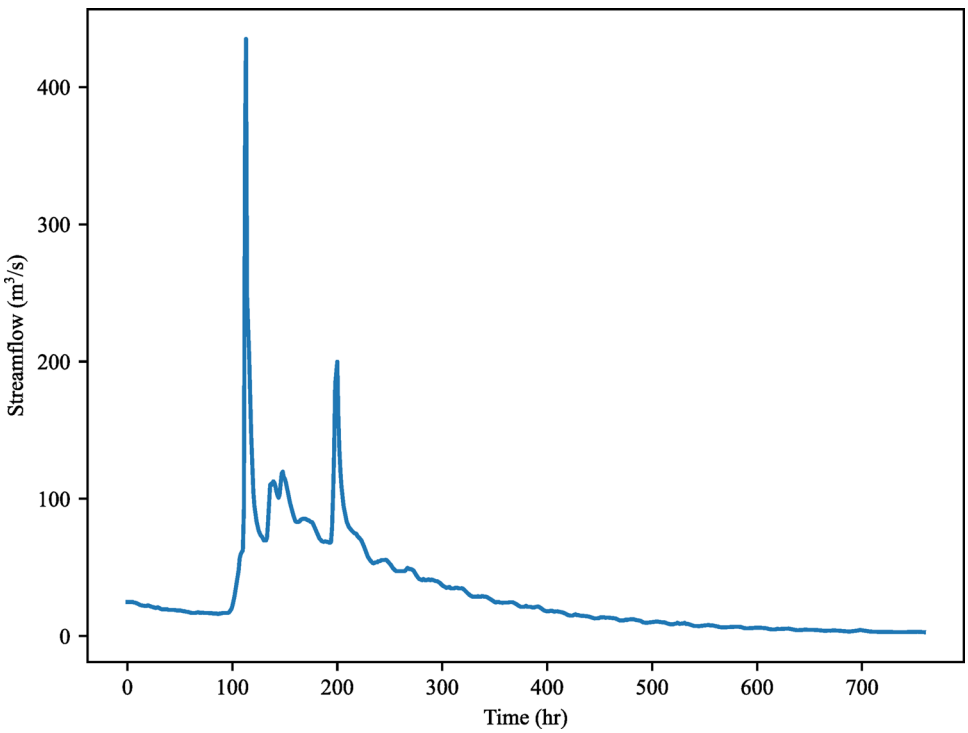

found in the original extended dataset. After determining the best-performing wavelet for the single summer recession, the detrending method is scaled to the entire dataset. This involves applying the modified DWT or process to the entire dataset to perform a comprehensive detrending.

4 Results and discussion

This study utilises both synthetic and real streamflow data to assess the effectiveness of a wavelet-based detrending method. Unlike synthetic data, where the added signal can be directly compared to the extracted components, real data present additional complexities due to external hydrological influences. A similar methodological framework, including wavelet detrending and wavelet selection, is applied to both datasets. Results of each process are first presented and discussed for the SS dataset followed by RS. The RS is also subjected to CWT-based extraction, after which the results are compared with those manually identified.

4.1 DWT detrending

4.1.1 Wavelet decomposition

Figures 7 and 8 show the decomposition process of the synthetic signal SS and observed streamflow RS, respectively. The DWT decomposition of the synthetic signal using wavelet "sym15" is further detailed to show the division of the parent signal into detail and the approximation sub-signals at each decomposition level. The approximation coefficient results from low-pass filtering and represents information on all the low-frequency components at each level. For example, at level 1, the scale is set as $2^1 = 2$, and the frequency content is halved fs/2. The approximation coefficient, cA1, represents a smooth version of the signal and contains all the components with a frequency range of (fs/2 → 0). Similarly, the approximation coefficient at the last decomposition contains the slowest-moving components (trend) of the original signal with a frequency range of (fs/32 → 0). In conclusion, pyramid-like decomposition provides a multiresolution analysis of a signal, allowing for the examination of its frequency content at different scales.

For the actual streamflow signal, the DWT plots using the wavelet "bior6.8" are shown in Fig. 8. The DWT results in five decomposition levels, each representing the signal attributes at a different resolution scale. The separation into multiple resolution levels is crucial in revealing the significant changes in non-stationary signals like streamflow—the abrupt changes in the detailed coefficients correspond to the rapid changes in the streamflow due to the sudden precipitation events. As we move upward in the decomposition levels, the detailed coefficients become more refined, locating short-term signal variations. On the other hand, the approximation coefficient is smooth and captures the long-term pattern or trends in the streamflow signal.

4.1.2 Wavelet shrinkage and reconstruction

The detailed coefficient from DWT is then subjected to wavelet thresholding (Fig. 9). The thresholding process converts the original coefficient array into modified coefficient arrays. The detail coefficients whose values do not meet the threshold criteria are truncated. The threshold adjustment is more frequent at higher frequency levels, where almost 95% of the values become zero.

DWT decomposes the hourly streamflow data containing at least one recession event into four lower-resolution levels. The detail components denoted from cD1 to cD4 represent the sub-signals having a period of 2 h to 32 h, respectively, with the periods increasing as we move down the resolution level. Hence, the detailed components at lower resolution levels have lower frequencies than those at higher decomposition levels. The approximation coefficient cA4 represents the signal's slowest changing component at the sixth decomposition level. There is a sharp rise in the magnitudes of coefficients around the time of the peak flow, representing the magnitudes of high-frequency noises associated with the peak flow event.

Figure 9 shows the inverse DWT process, where the trend is reconstructed from the modified set of detail coefficients. A sub-signal of the primary signal is obtained using the *waverec* command in the pywt python module. The reconstructed signal is free from all the high-frequency noise components and represents the underlying trend of the primary signal. A detrended signal is then obtained by subtracting the trend from the primary signal.

Likewise, the following stem plots (Fig. 10) show wavelet thresholding results for the four decomposition levels of Coif5 using the Garrotte threshold rule. The left column shows the log values of the unmodified detailed coefficients, while the right column has threshold-adjusted values against the corresponding resolution level. The stem plots provide a visual representation of the thresholding process. In these plots, the retained coefficients in the right column indicate parts of the signal that are believed to contain essential information, while the eliminated coefficients in the left column signify areas deemed to contain noise. The approximation coefficient is left unchanged as it is believed to contain only the trend information. The resulting thresholded coefficients then be joined with the approximation coefficient to obtain the denoised signal representing the underlying trend of the primary signal.

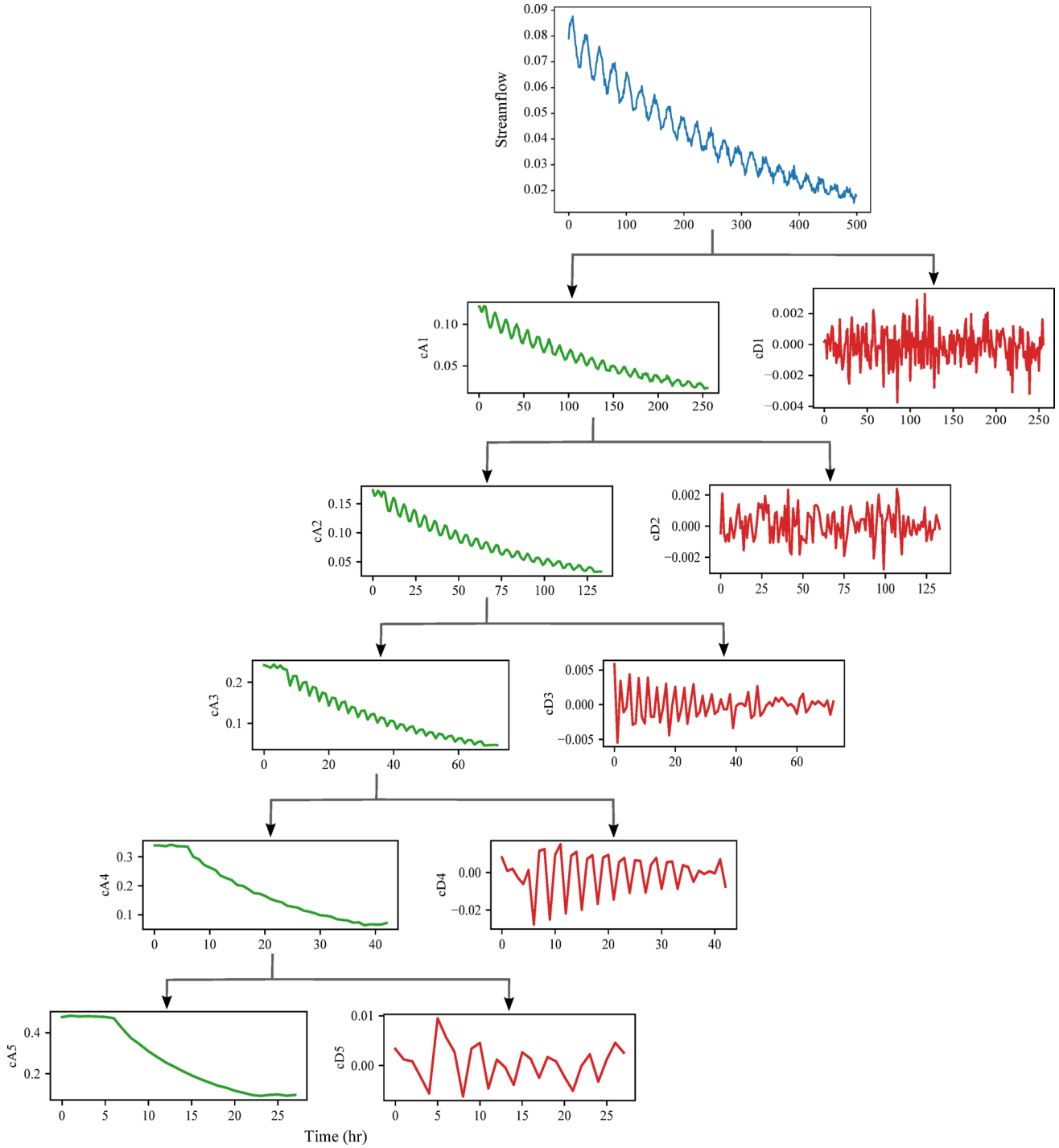

Fig. 7 DWT workflow for the synthetic diel signal. The original signal is decomposed into a pair of detail and approximation coefficients. The approximation coefficient then undergoes further vision at each level, revealing the finest details in the signal

The stemplots can be tweaked by adjusting the thresholding criteria. The threshold criteria work as a trade-off between noise reduction and the preservation of signal details and depend on the type of application. The selection of optimal wavelet type and thresholding criteria can ensure a more efficient denoising process, resulting in a cleaner, clearer signal with the essential features intact.

Finally, the trend is reconstructed from these thresholded arrays of coefficients. The detrending results from the wavelet threshold method and the moving average are shown in Fig. 11. The wavelet-based trend excels at adapting to sudden

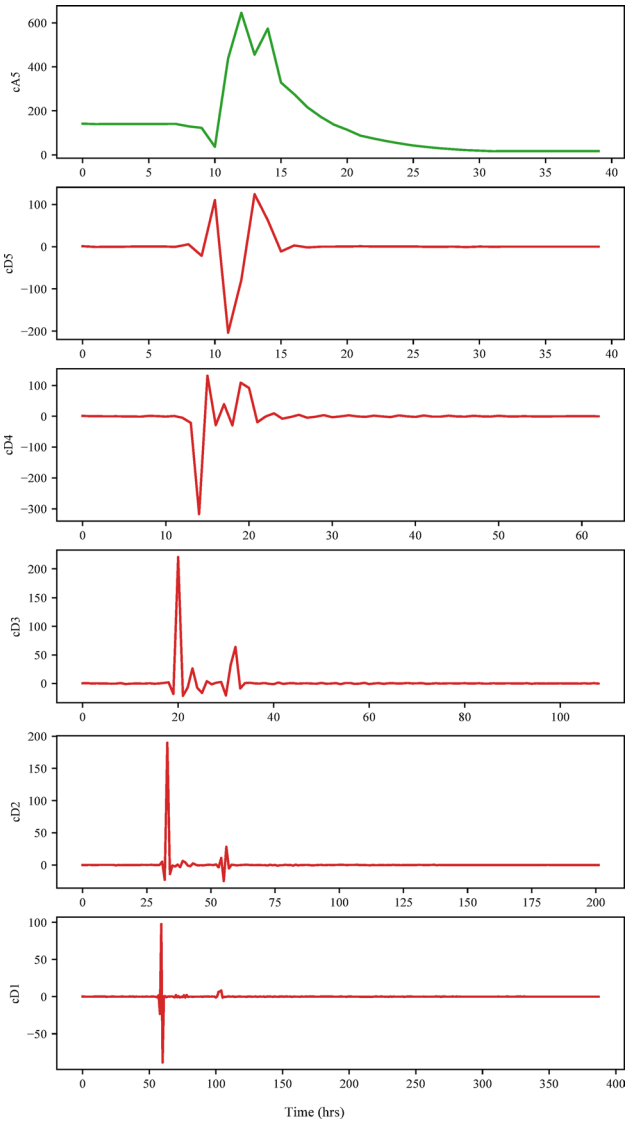

Fig. 8 The maximum level DWT decomposition of the real-life observed streamflow. The detailed coefficients represent the noise or short-term fluctuations at each level, while the approximation coefficients exhibit the long-term trend in the signal

signal spikes, as the threshold-adjusted detail coefficients preserve peak magnitudes, ensuring a more precise depiction of transient fluctuations that the moving average often smooths over. This flexibility arises from DWT's capability to break down signals into various frequency bands, adeptly capturing both short-term changes and long-term patterns—traits that render it especially suitable for non-stationary signals featuring dynamic variations, like the RS dataset. In contrast, the moving average, while computationally simple and effective for stationary signals like the synthetic signal (SS), struggles to retain critical high-frequency components in non-stationary scenarios, risking the loss of key signal features due to its rigid smoothing approach. DWT's flexibility, though computationally demanding and requiring careful wavelet and threshold selection, offers a clear advantage in preserving signal integrity and variability, especially in complex, noisy conditions where the moving average's simplicity becomes a limitation.

4.1.3 Performance evaluation of optimal wavelet

Wavelet detrending analysis, comprising wavelet decomposition and thresholding, is conducted for each mother wavelet from the discrete wavelet family, evaluated across three thresholding rules: hard, soft, and garrotte. Table 1 presents the coefficient of determination (R^2), signal-to-noise ratio (SNR), and root mean square error (RMSE) for the moving average method and the three top-performing wavelets under each thresholding type.

For the synthetic signal (SS), SNR and correlation analyses indicate that DWT method achieves denoising performance comparable to the moving average in extracting diurnal fluctuations from a recession signal. Among the wavelets tested, the 'sym15' wavelet with hard thresholding yields the highest correlation and SNR values, demonstrating its superior ability to isolate the artificially introduced oscillatory noise. A detailed breakdown of the wavelet transform for 'sym15' is provided in subsequent sections. This consistency in SS highlights the robustness of DWT under controlled conditions where noise characteristics are known and stationary, aligning well with the moving average's strengths in handling simpler, synthetic signals.

In contrast, for the real-world streamflow (RS) dataset, the moving average method performs poorly, with an R^2 near zero, a high RMSE, and a low SNR, reflecting weak correlation with the lagged ET reference signal, significant error, and poor signal-to-noise quality. This suggests that the moving average struggles to capture diurnal fluctuations amidst the non-stationary trends and high-frequency noise introduced by precipitation events in the baseflow time series. Conversely, DWT denoising significantly outperforms the traditional approach. For example, the 'bior6.8' wavelet with the garrotte threshold achieves an R^2 of 0.3477, an RMSE of 0.5002, and an SNR of 91.6488, markedly surpassing the moving average's results. This underscores DWT's effectiveness in managing complex, noisy, and non-stationary signals typical of real-world data, where traditional smoothing methods like the moving average falter.

The consistency of results between SS and RS reveals both strengths and limitations. For SS, both DWT and the moving average perform reliably due to the synthetic signal's stationarity and controlled noise, with DWT (e.g., 'sym15') offering a slight edge in precision. However, in RS, the performance diverges sharply: the moving average's simplicity becomes a limitation when confronted with

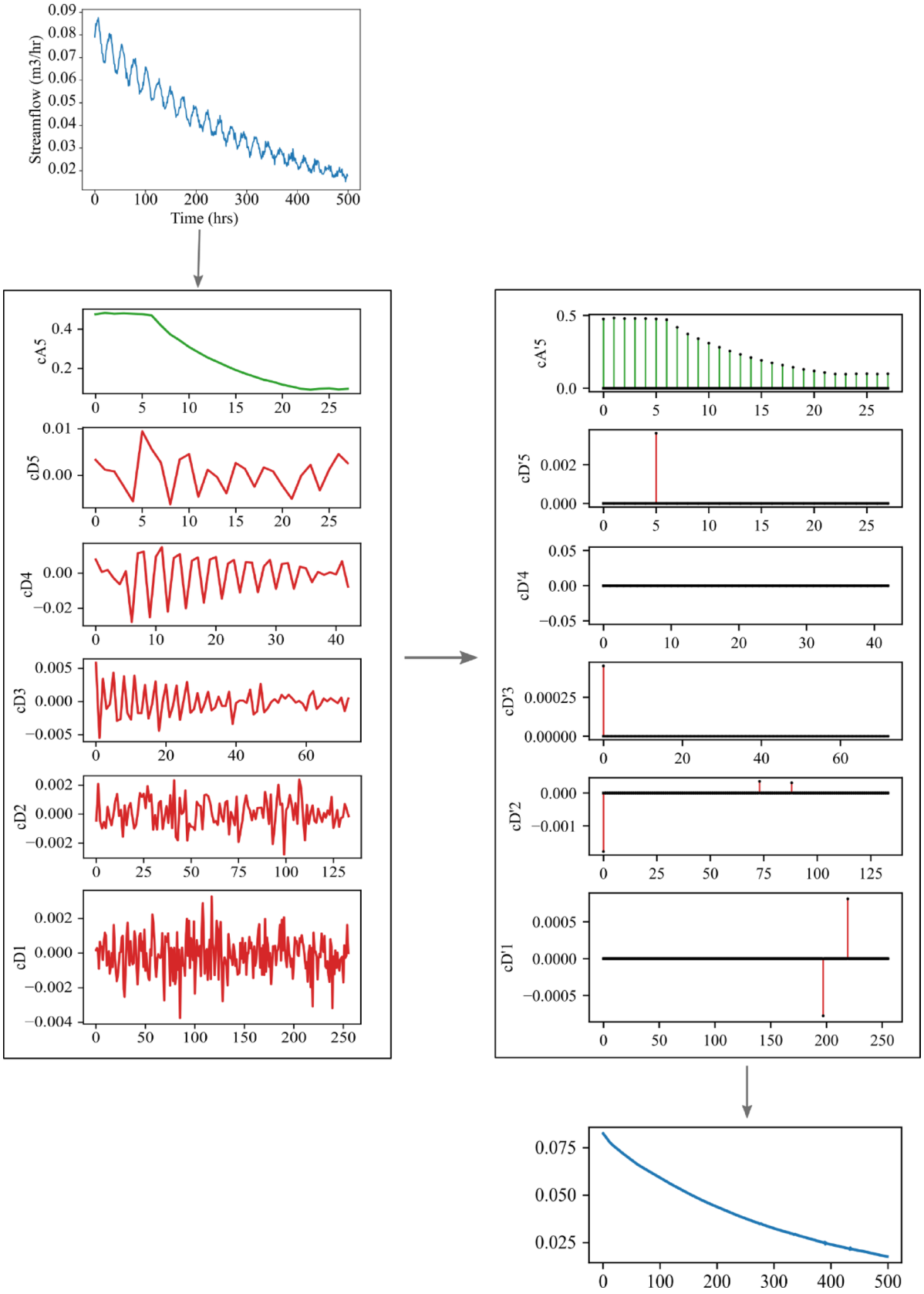

Fig. 9 Wavelet-aided thresholding to denoise each decomposed coefficient of the signal, followed by the reconstruction of the denoised signal representing the underlying trend

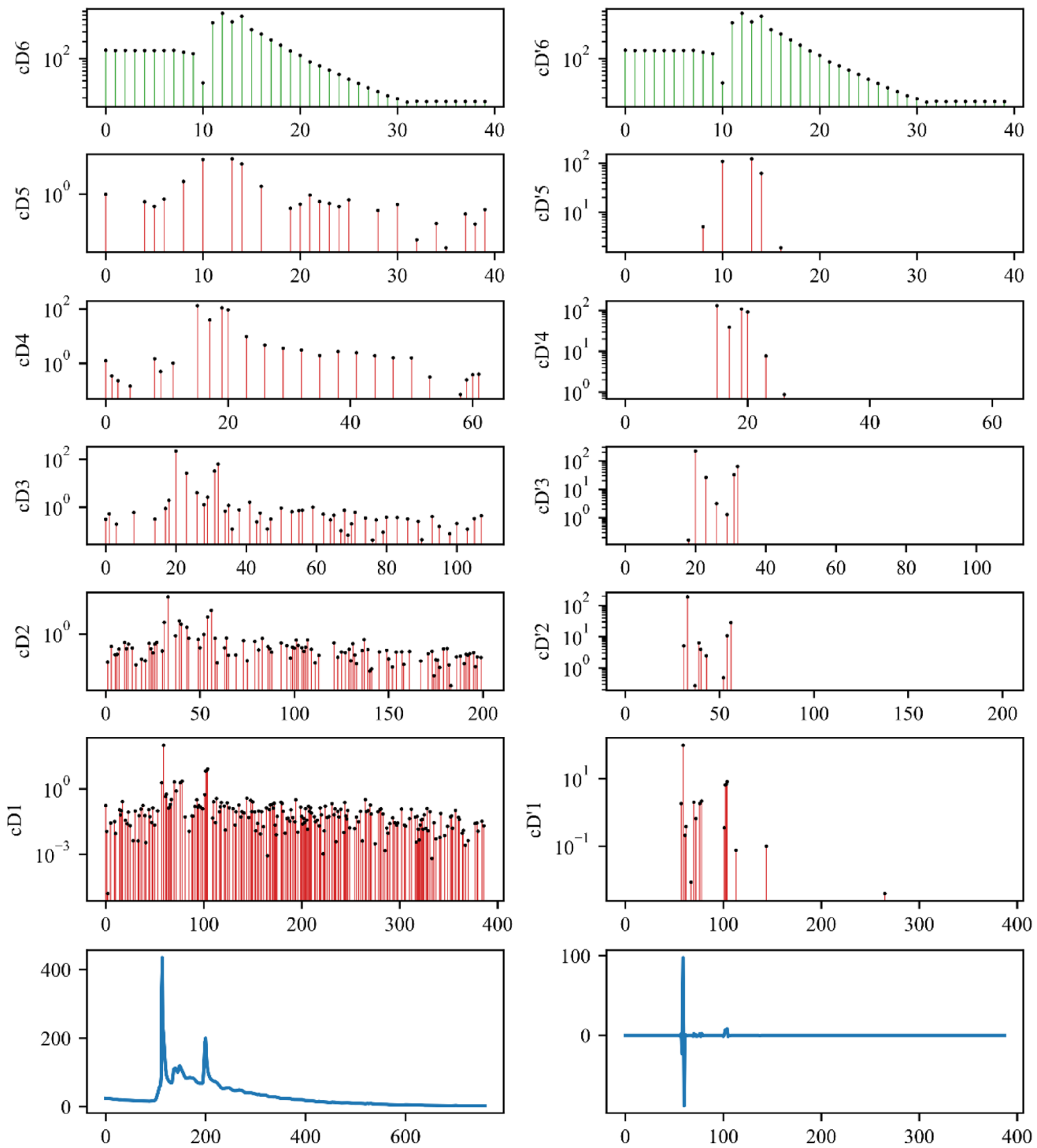

Fig. 10 Amplitudes of the DWT coefficients of the observed streamflow signal (left) and the threshold adjusted coefficients(right)

non-stationary dynamics, while DWT adapts effectively, as evidenced by the 'bior6.8' results. This discrepancy highlights that DWT's flexibility in wavelet selection and thresholding makes it more versatile across diverse signal types. In contrast, the moving average is better suited to stationary signals with consistent trends. Limitations in RS, such as irregular noise from precipitation or unmodeled environmental factors, could still compromise DWT's results, though its performance remains superior. These findings suggest that while DWT consistently outperforms traditional methods, its efficacy in real data depends on

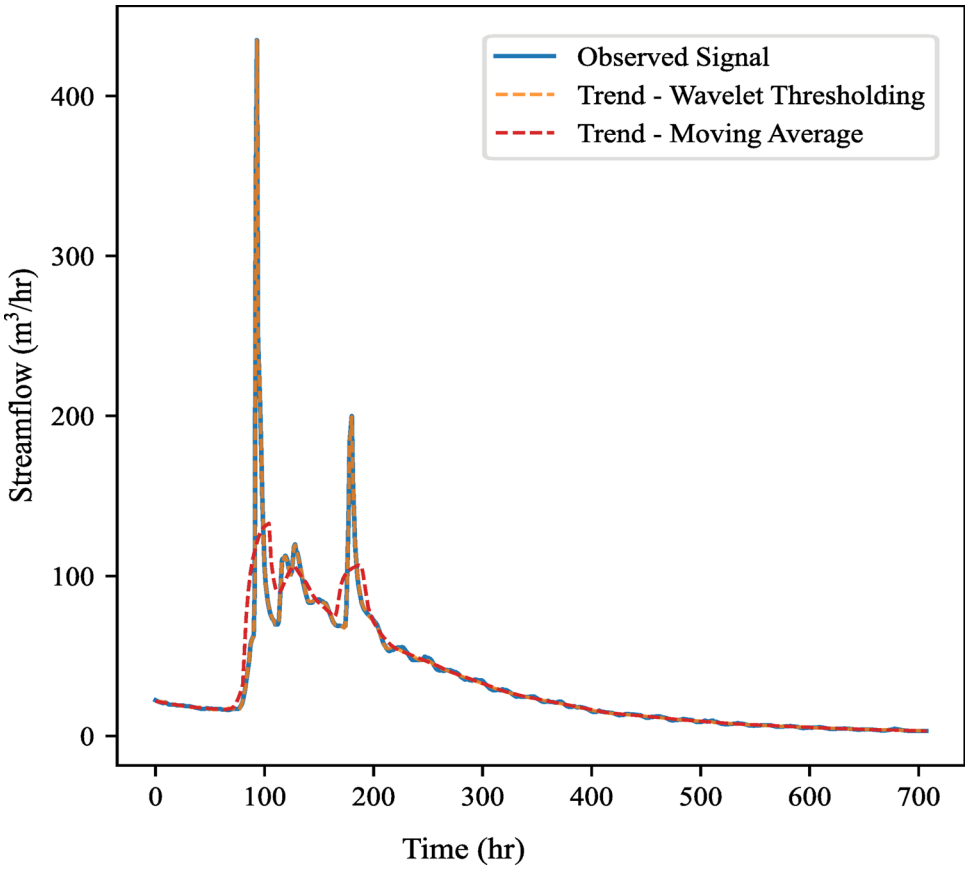

Fig. 11 Comparison between detrended signals using wavelet threshold and moving average methods

Table 1 R^2, MRSE, and SNR values for SS and the best-performing wavelet basis function

Signal	Wavelet	Threshold	R^2	MSRE	SNR
SS	Moving average		0.9996	0.0015	68.53
	sym15	Soft	0.9994	0.0017	65.88
	sym15	Hard	0.9963	0.0015	68.50
	sym15	Garrotte	0.9991	0.0017	66.75
RS	Moving average		0.0009	18.59	19.35
	coif8	Soft	0.1166	0.7698	83.03
	coif8	Hard	0.1166	0.7698	83.03
	bior6.8	Garrotte	0.3477	0.5002	91.65

careful wavelet and threshold selection tailored to the signal's specific non-stationarities.

The appendix provides a complete list of the performance metrics of all of the 106 wavelets for both datasets.

It is to be noted that the choice of the "bior6.8" wavelet was based on its strong performance in capturing diurnal fluctuations in the specific RS dataset. However, wavelet-based detrending is inherently data-dependent, as various hydrological conditions, noise levels, and signal structures can influence the selection of the optimal wavelet and thresholding method. While "bior6.8" has proven effective for this dataset, other wavelets may perform better under different circumstances. This study emphasises a flexible framework where wavelet selection is guided by performance metrics rather than a fixed choice, ensuring adaptability to diverse datasets. Future research should evaluate the approach across a variety of hydrological datasets to determine its broader applicability and identify potential limitations in different contexts.

4.2 CWT analysis

4.2.1 Wavelet power spectrums

The CWT analysis presents us with multiple graphs, which can help us identify the frequencies and times where the diurnal fluctuations were present in the primary signal. The typical CWT analysis of the observed streamflow signal is presented in Fig. 12

The parameters for the continuous wavelet analysis are adopted from (Torrence and Compo 1998) set as $\delta t = 1$ h since our data is hourly distributed. The first scale, *SS,* is 2 h because $s = 2\delta t$ and $\delta j = 0.25$ to do 4 sub-octaves per octave (scale level). Moreover, j equals 11 to plot the graph to up to eleven powers of two.

The first plot (Fig. 12b) shows the wavelet transform's power (absolute value squared) for the hourly detrended streamflow at different scales and times. The power is represented by a colour scale, with higher power areas being

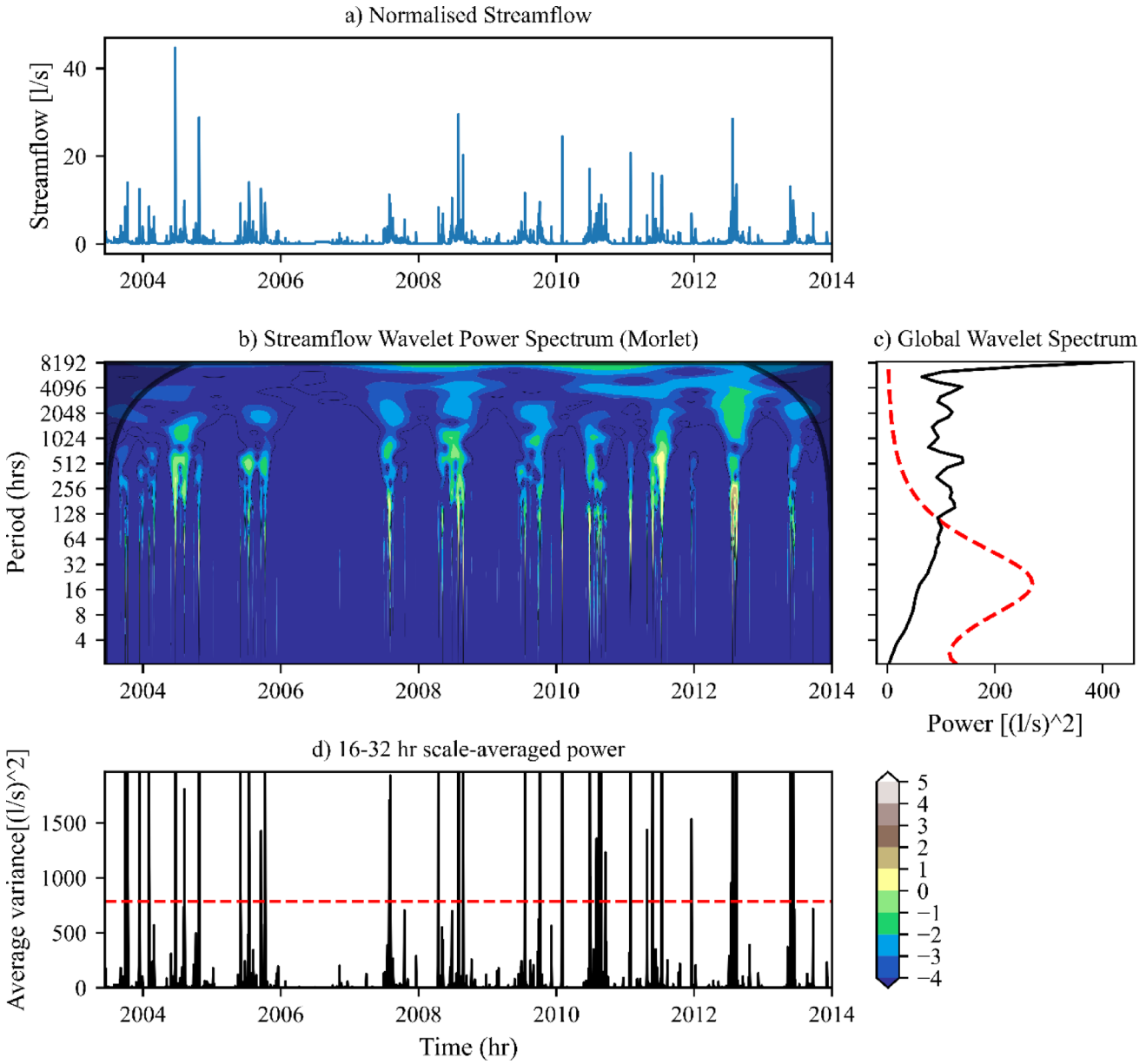

Fig. 12 CWT analysis of the observed streamflow time series. The time series and wavelet power spectra are shown in (**a**) and (**b**). The scalogram represents the strength of power ($\log_2$) in the contour image in (**b**). **c** Shows the global wavelet spectrum with a 95% significance line in the red dotted line. **d** Represents a 16–32 h. scaled average wavelet with a 95% significance line

more yellow, while lower wavelet powers scale towards blue. The red contours correspond to the 95% significance level drawn against a red noise background spectrum. The red noise corresponds to the signal's autocorrelation with a lagged-1 version of itself and represents the expected power at each frequency in the absence of any accurate signal (Torrence and Compo 1998).

$$x_n = \alpha x_{n-1} + z_n \tag{16}$$

where α is the lag-1 autocorrelation of the time series, and z_n is Gaussian white noise.

The shaded region is the cone of influence, inside which the distortion due to edge effects is significant. These edge effects occur at the wavelet spectrum's beginning and end because of zero padding.

The second CWT plot (Fig. 12c) shows the global wavelet spectrum (GWS), which is a helpful tool for determining the most dominant frequency in the primary signal. It is constructed by integrating the wavelet power spectrum across all time points for each scale. The peaks in GWS correspond to the scales at which the signal has the most power or energy. GWS can also be used for significance testing, where the GWS is compared against a specified background

noise model. In Fig. 12c, the red line represents the 95% significance level against a red-noise background spectrum.

The third CWT plot (Fig. 12d) shows the scale average variance (SAV), which measures the strength of signal fluctuations over a specified range of scales. It is obtained by averaging the CWT power spectrum across various scales of interest. It can help identify times of particularly strong or weak fluctuations in the signal over the range. The scaled-powered average's statistical significance is also assessed by comparing it against a 95% confidence level. Both the wavelet power spectrum and the scaled power average are used to identify and filter the timestamps of significant noise in the signal.

4.2.2 CWT analysis of detrended signals

4.2.2.1 Moving average Figure 13b shows the wavelet transform's power (absolute value squared) for the hourly streamflow at different scales and times. As can be seen from Fig. 13b. Due to incomplete detrending, the moving average produces an undesirable boost in power for certain regions while other regions are attenuated in the wavelet spectrum.

The global wavelet power of the moving average-detrended signal (Fig. 13c) has a huge peak amplitude, which masks the peaks of higher frequencies. Although the

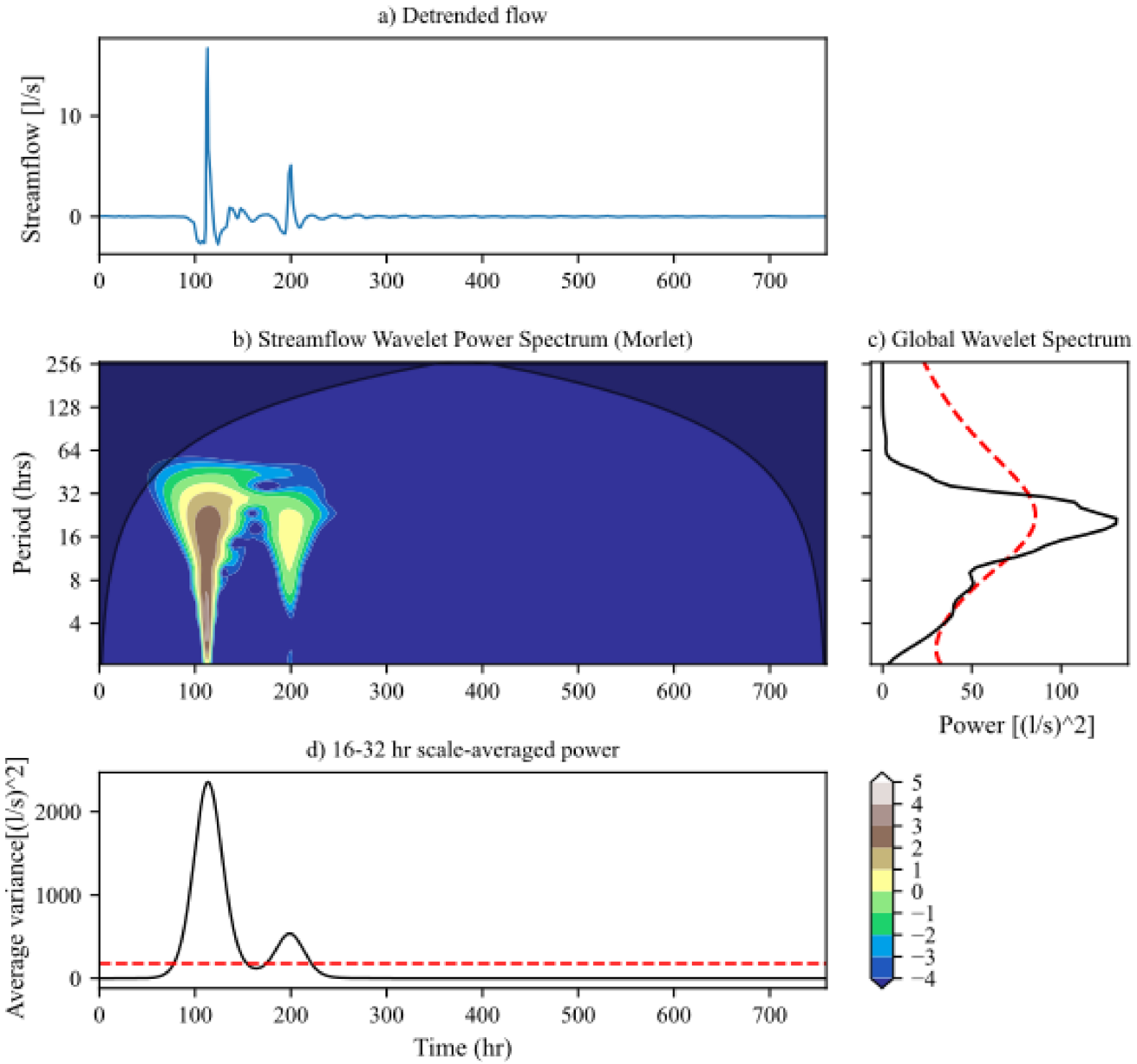

Fig. 13 CWT of the moving average detrended signal

peak is observed in the diel region, it has a broad base and is intersected by the 95% significance level line in the global wavelet power plot.

The SAV subplot (Fig. 13d) shows the time series of the average signal variance inside the diurnal frequency range. The time series for the 16–32 h scaled averaged power has two statistically significant peaks corresponding to the two power concentrated regions in the wavelet power spectrum. In contrast, the average variance for the rest of the region stays below the significance level, which tells us very little about the evolution of the diurnal signal with time.

4.2.2.2 Wavelet detrending The "bior 6.8" wavelet was chosen for detrending purposes, with a decomposition level of 4. The garrotte threshold rule is used to remove noise in each decomposition level. The combination of wavelet type and threshold rule has been seen to perform best when detrending the real-life observed streamflow signals to extract diurnal fluctuation. Represents the wavelet scalogram of the thresholded detrended signal.

A good spread of wavelet power across the entire series length shows the ability of the wavelet threshold algorithm to extract diel signals from non-stationary streamflow data sets having precipitation events. The global wavelet power (Fig. 14b) has a sharp peak concentrated in the diel region, and its magnitude goes well above the 95% confidence level. This peak represents the strength of diel oscillations in the signal. The GWS (Fig. 14c) of the wavelet-aided detrended signal has a minimal peak amplitude compared to the moving average, which again shows a better detrending performance of the DWT method for extracting diurnal fluctuations.

The SAV plot (Fig. 14d) for the 16–32 h band remains above the 5% significant levels, representing the strength of the diel fluctuations in those regions. The time series of scaled average variance shows the temporal location of the events, which are responsible for the peaks shown in the global power spectrum. Moreover, the decay in the diel signal peaks is replicated in the scaled average variance for the 16–32 h band for the wavelet-aided detrended signal. On the time series of scaled average time series, there is a rise in the variance at the time of the rainfall event, whereas the variance throughout the signal remains significant. In conclusion, the continuous wavelet analysis of the wavelet-detrended signal shows improved results where a power concentrated spread uniformly across the length of the data set. The scaled average variance also shows an excellent distribution above the significance level.

4.3 Extraction of diurnal episodes

The CWT plots of the detrended signals give us a deeper insight into the variability in the power and variance of diel fluctuations inside the signal and help extract diurnal episodes from the signal. The extracted diurnal signals are also subjected to the prescribed filtering criteria, followed by manual inspection (Fig. 15).

Finally, the extracted signals are validated by comparing them with the manually identified diurnal episodes in the same data set by Sarwar et al. (2022).

The comparison reveals that the diurnal episodes extracted through CWT analysis overlap the manually extracted signals on several occasions (27/41); however, there are instances where the diurnal episodes differ.

There could be several reasons for this observed discrepancy between CWT and manually extracted diurnal episodes. These include signal noise, phase variability, or the presence of overlapping periodicities that obscure the 24-h cycle, such as harmonic frequencies or irregular external influences (Flinchem and Jay 2000; Anbalagan et al. 2023). To investigate these factors and quantify their impact, we applied Fourier Transform (FT) analysis with Full Width at Half Maximum (FWHM) assessment to the manually extracted episodes that diverged from CWT results. The FT decomposes the signal into its frequency components, revealing the strength and distribution of periodicities (e.g., 6-h, 12-h harmonics), while FWHM measures the sharpness of these spectral peaks. A narrow FWHM indicates a well-defined frequency, such as a dominant harmonic, whereas a broad FWHM suggests energy spread across multiple frequencies, signalling interference or a weakened diurnal component (Inouye et al. 1969; Locci-Lopez et al. 2018).

One primary reason is the presence of harmonic frequencies (e.g., 6h, 12h, etc.) that complicate the signal. Manually identified diurnal episodes may resemble a waveform but are dominated by strong harmonic presence which overshadows or interferes with the 24-h component. On the other hand, the CWT method is designed to isolate true diurnal fluctuations, targeting a dominant frequency of approximately 24 h.

- In many differing cases, harmonic frequencies were detected with amplitudes exceeding 50% of the diurnal signal's amplitude, posing challenges for the CWT's ability to isolate the 24-h component. For example, the FFT analyses of the manual diel episode: September 1, 2008, to September 9, 2008, in Fig. 16 shows a strong harmonic period (12.357 h) present along with the main diurnal period (24.83 h), which causes the CWT method to discard this based on the filtering criteria.

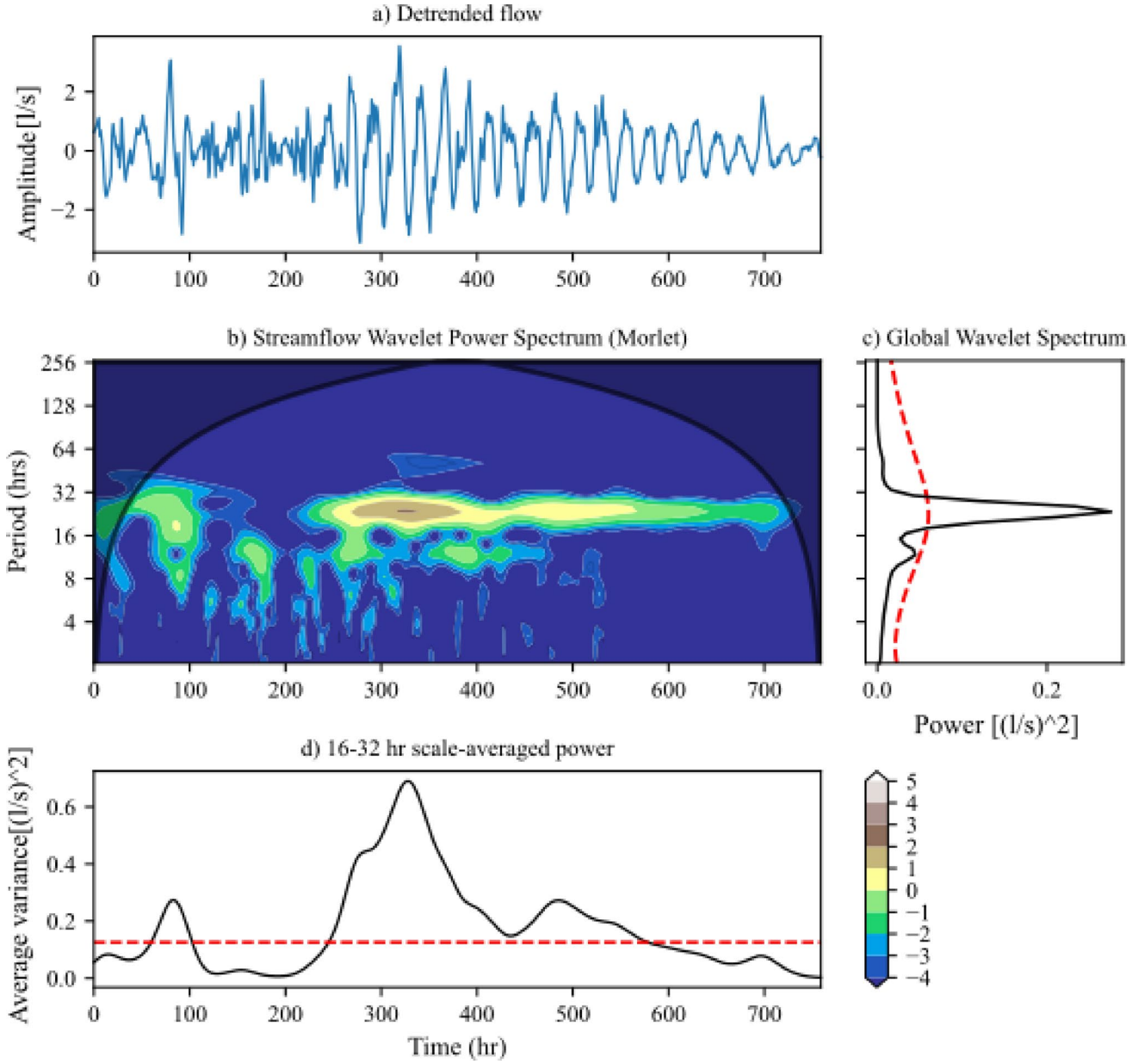

Fig. 14 CWT of the detrended signal via wavelet-aided thresholding

- On other occasions, like the manually identified diel episode from October 10, 2008, to October 15, 2008, FT analysis revealed a dominant 12-h period rather than the expected 24-h cycle. The power spectral density (PSD) showed a sharp peak at 12.1 h with a narrow FWHM, indicating a well-defined harmonic signal. This strong harmonic presence likely masked the diurnal component, causing the CWT method to misclassify these episodes as non-diurnal. These findings support the argument that discrepancies stem from signal complexity—specifically, the overlay of harmonic frequencies—rather than an inherent flaw in the CWT methodology.

A second category of discrepancies involves episodes with a weak diurnal peak and a broad FWHM. In these cases, the PSD exhibits a wide peak around the 24-h frequency, signifying that the signal's energy is distributed across a range of frequencies rather than concentrated at 24 h. This broadening could result from interference (e.g., noise or overlapping cycles like 12-h or seasonal periods), distortion, or damping of the diurnal oscillation. For example, a broad FWHM might reflect a diurnal signal diluted by meteorological variability in environmental data (Fig. 17).

In the CWT analysis, such episodes were excluded because the diurnal frequency's amplitude was found not statistically significantly higher than neighboring frequencies

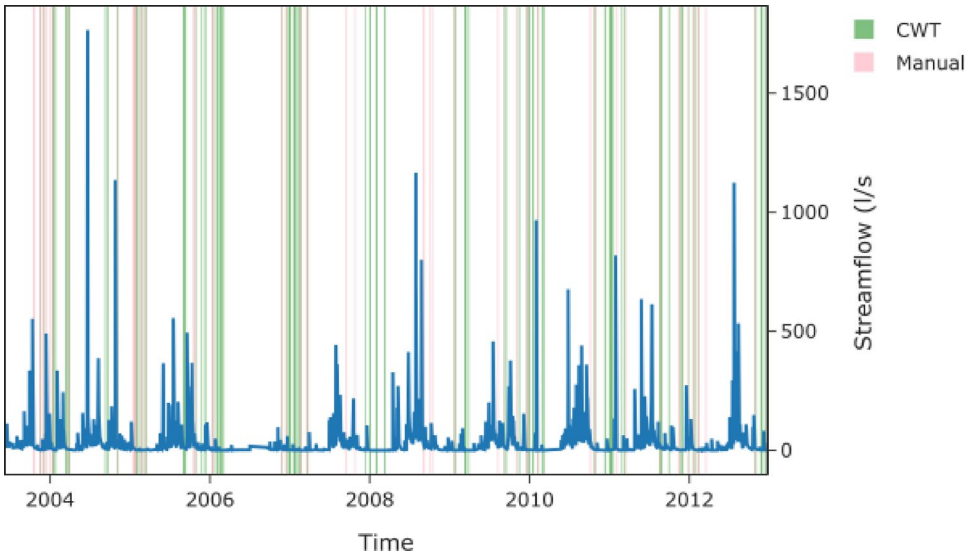

Fig. 15 Comparison of the diurnal episodes: manually extracted (Pink Bars) vs. the CWT method (Green Bars)

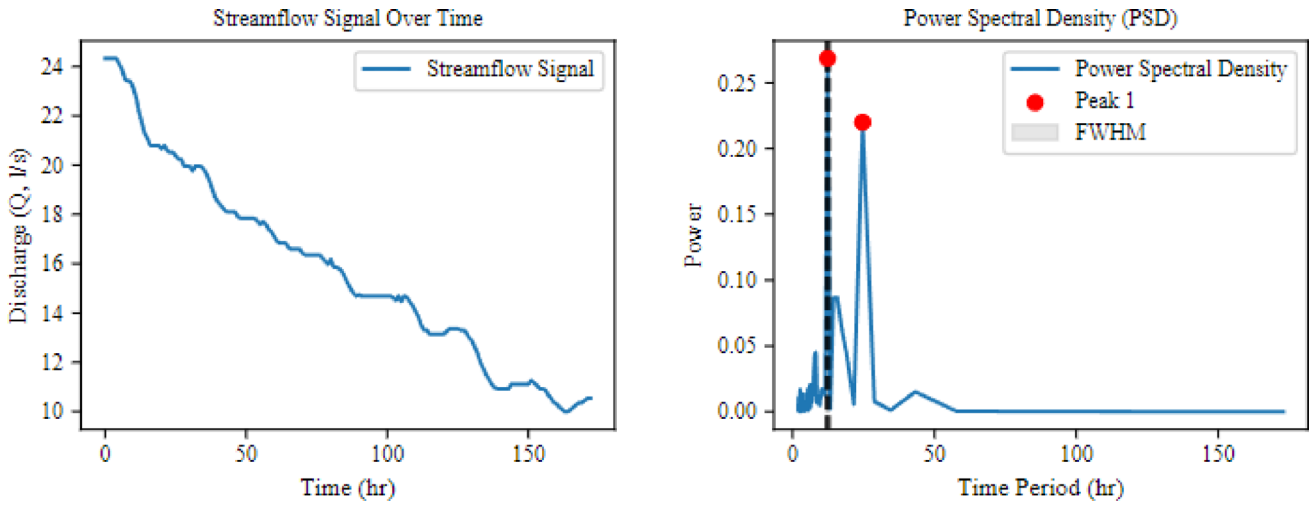

Fig. 16 Falsely identified (manual) diel episode exhibiting strong harmonic interference

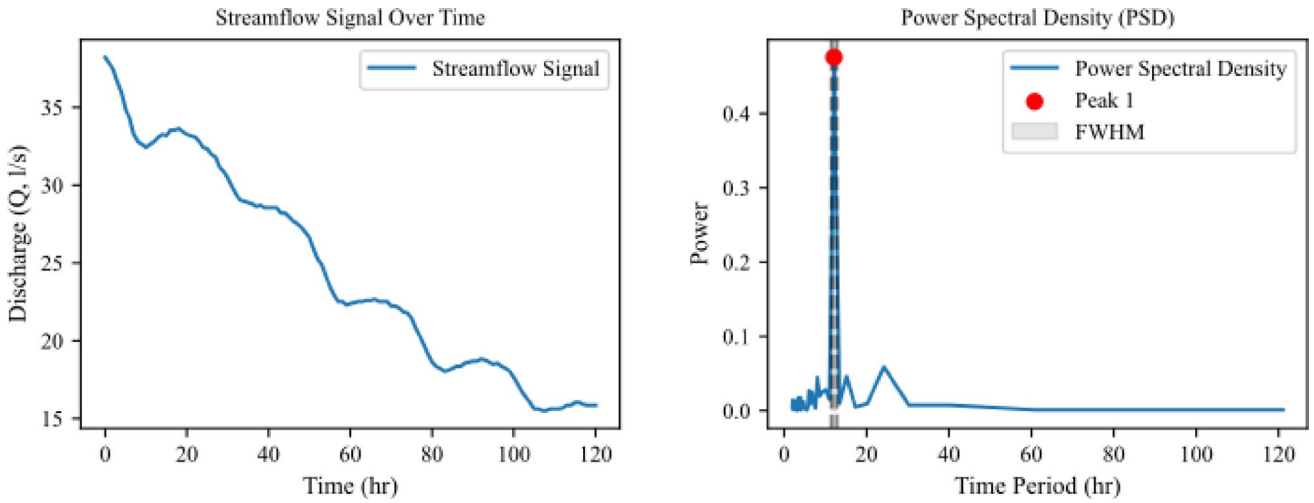

Fig. 17 A wavelike diel form with a dominant harmonic frequency, correctly classified by CWT as non-diurnal

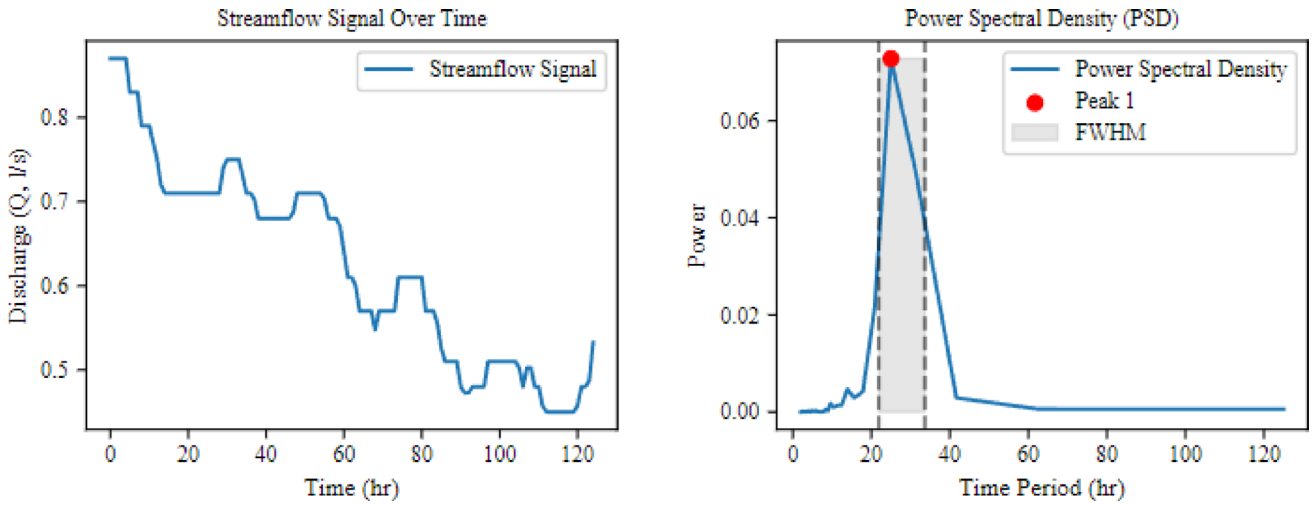

Fig. 18 Weak diel episode with broad FWHM and diffused diurnal signal

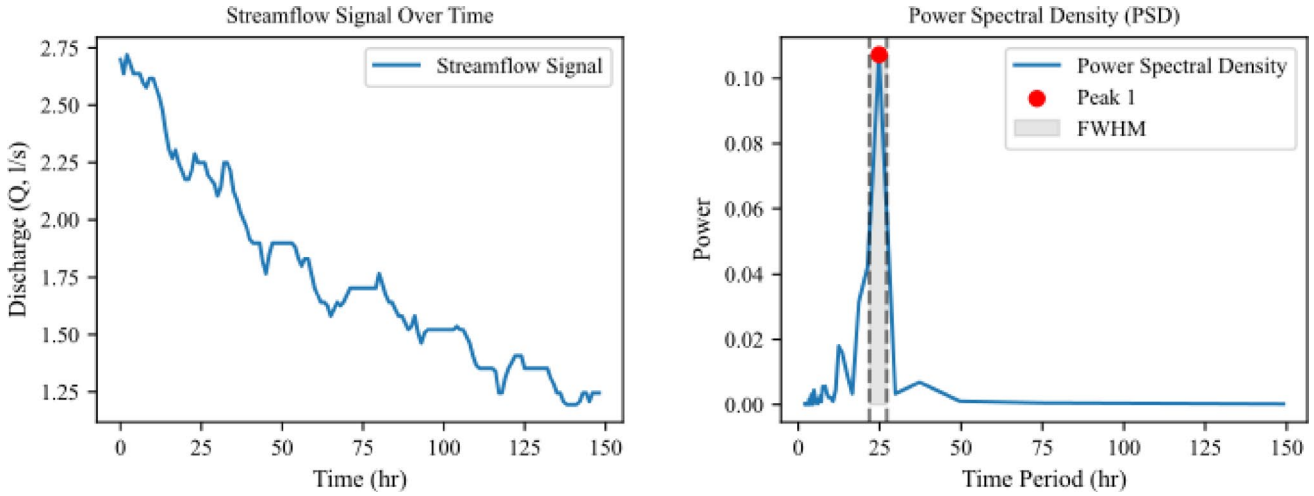

Fig. 19 CWT-detected diel episode with a strong frequency signal but weak visual pattern

(e.g., Z-score < 2 and p-value > 0.05). This filtering reflects the method's stringent criteria for identifying robust diurnal patterns. Still, it also highlights a limitation: the CWT struggles to detect weak or diffused diurnal signals, which manual extraction might still flag based on subjective interpretation. One such episode is presented in Fig. 18, which shows a weak diel episode from March 16, 2012, to March 19, 2012.

We also analysed episodes missed by the manual method but detected by CWT. This category includes diel episodes that lack an obvious pattern to the naked eye but are confirmed through FT analysis to exhibit a strong diel frequency. Figure 19 presents an example from November 25 to December 1, 2007, where the FT reveals a dominant period of 24.83 h, indicating a clear diurnal signal despite its subtle appearance in the raw data.

The frequency resolution of the CWT method is crucial for effective diurnal signal extraction. While different resolutions are tested, they may not always fully separate closely spaced harmonics from the diurnal frequency, particularly when these harmonics fall within its range. To evaluate CWT's robustness and determine whether discrepancies stem from data limitations rather than the method itself, we conducted a sensitivity analysis.

We re-ran CWT on discrepant cases, varying the number of sub-octaves per octave from 4 to 8 to compare finer (higher sub-octave) and coarser resolutions. Detection against manual extraction improved in only 2 (14.23%) of 14 cases, with finer scales slightly enhancing 24-h signal isolation in moderate harmonic interference. However, residual discrepancies persisted due to harmonic overlap (e.g., 12-h periods) and broad FWHM, confirming that interference—not scale resolution—limits performance. These findings reinforce CWT's robustness when an appropriate detection window is used.

Despite these challenges, the proposed CWT method successfully extracted a significant number of diurnal episodes, even detecting oscillations missed by manual extraction—likely due to oversight or other limitations. This comparison underscores the complexities of analysing diurnal fluctuations and the need to account for harmonic frequencies and frequency resolution in extraction methods. It also highlights CWT's complementary nature, as it can reveal diurnal patterns that manual methods may overlook. It also highlights the complementary nature of the CWT method, which can uncover diurnal patterns that may go unnoticed through manual extraction alone.

5 Conclusion

Wavelet analysis is used in this paper to extract and analyse diel fluctuation from a streamflow signal. A detrending scheme based on wavelet-aided thresholds is used to extract dial signals from streamflow sessions and a workflow to choose the best wavelet. The wavelet-aided threshold method was also pitted against the most widely used moving average method. Based on the comparison with the moving average and the results of the CWT, it was seen that the WT detrending scheme was better able to follow sudden peaks in the stream flow and that the detrended data had a more uniform power spectrum as compared to the detrended signal obtained from the moving average. The global wavelet spectrums also provided wavelet powers of the detrended signals against the mean, that the noise spectrum. Lastly, the scale average time series of the average variance of the signal provided the temporal distribution of variance inside a specific frequency band. They helped identify the exact timestamps of the event carrying the most variance in the frequency band.

Appendix

Wavelet performance matrices for the synthetic signal.

Sr. No	Wavelet	R^2	RMSE	SNR	Tmax (hr)	R^2	RMSE	SNR	Tmax (hr)	R^2	RMSE	SNR	Tmax (hr)
		Soft				Hard				Garrote			
0	bior1.1	0.7018	0.0100	30.7204	250.0000	0.7002	0.0100	30.8285	250.0000	0.7019	0.0100	30.7528	250.0000
1	bior1.3	0.9805	0.0031	54.1665	62.5000	0.9811	0.0030	54.4981	62.5000	0.9806	0.0031	54.2333	62.5000
2	bior1.5	0.9952	0.0022	60.7466	23.8095	0.9954	0.0022	61.4578	23.8095	0.9953	0.0022	60.9464	23.8095
3	bior2.2	0.9990	0.0019	64.1988	23.8095	0.9982	0.0019	64.2502	23.8095	0.9989	0.0019	64.3357	23.8095
4	bior2.4	0.9996	0.0019	64.3508	23.8095	0.9993	0.0018	64.6162	23.8095	0.9995	0.0019	64.3979	23.8095
5	bior2.6	0.9997	0.0018	64.4994	23.8095	0.9987	0.0017	65.9353	23.8095	0.9997	0.0018	64.6020	23.8095
6	bior2.8	0.9996	0.0018	64.6903	23.8095	0.9996	0.0018	64.6903	23.8095	0.9996	0.0018	64.6903	23.8095
7	bior3.1	0.9877	0.0026	57.3994	23.8095	0.9887	0.0026	57.7566	23.8095	0.9892	0.0026	57.9872	23.8095
8	bior3.3	0.9987	0.0019	63.6968	23.8095	0.9986	0.0019	63.6257	23.8095	0.9986	0.0019	63.6640	23.8095
9	bior3.5	0.9990	0.0019	64.2831	23.8095	0.9967	0.0019	64.3714	23.8095	0.9989	0.0019	64.4074	23.8095
10	bior3.7	0.9993	0.0019	64.2902	23.8095	0.9986	0.0019	64.2669	23.8095	0.9994	0.0019	64.3758	23.8095
11	bior3.9	0.9989	0.0018	64.8321	23.8095	0.9989	0.0018	64.8321	23.8095	0.9989	0.0018	64.8321	23.8095
12	bior4.4	0.9996	0.0019	64.3462	23.8095	0.9996	0.0019	64.3462	23.8095	0.9996	0.0019	64.3462	23.8095
13	bior5.5	0.9996	0.0018	65.0519	23.8095	0.9969	0.0016	67.2559	23.8095	0.9995	0.0018	65.5287	23.8095
14	bior6.8	0.9996	0.0018	64.7360	23.8095	0.9982	0.0017	66.2695	23.8095	0.9996	0.0018	64.8630	23.8095
15	coif1	0.9994	0.0019	64.1289	23.8095	0.9988	0.0018	64.6225	23.8095	0.9994	0.0019	64.3107	23.8095
16	coif2	0.9997	0.0019	64.4018	23.8095	0.9997	0.0019	64.4018	23.8095	0.9997	0.0019	64.4018	23.8095
17	coif3	0.9995	0.0018	65.0772	23.8095	0.9965	0.0015	68.1546	23.8095	0.9995	0.0018	65.3617	23.8095
18	coif4	0.9994	0.0018	64.9222	23.8095	0.9994	0.0018	64.9222	23.8095	0.9994	0.0018	64.9222	23.8095
19	coif5	0.9992	0.0018	64.7790	23.8095	0.9992	0.0018	64.7790	23.8095	0.9992	0.0018	64.7790	23.8095
20	coif6	0.9937	0.0012	72.9923	11.9048	0.9937	0.0012	72.9923	11.9048	0.9937	0.0012	72.9923	11.9048
21	coif7	0.9931	0.0011	74.6558	11.9048	0.9931	0.0011	74.6558	11.9048	0.9931	0.0011	74.6558	11.9048
22	coif8	0.9935	0.0012	73.3926	11.9048	0.9935	0.0012	73.3926	11.9048	0.9935	0.0012	73.3926	11.9048
23	coif9	0.9932	0.0011	74.3464	11.9048	0.9932	0.0011	74.3464	11.9048	0.9932	0.0011	74.3464	11.9048
24	coif10	0.9934	0.0012	73.6360	11.9048	0.9934	0.0012	73.6360	11.9048	0.9934	0.0012	73.6360	11.9048
25	coif11	0.9916	0.0009	79.5447	6.0241	0.9916	0.0009	79.5447	6.0241	0.9916	0.0009	79.5447	6.0241
26	coif12	0.9916	0.0009	79.5545	6.0241	0.9916	0.0009	79.5545	6.0241	0.9916	0.0009	79.5545	6.0241
27	coif13	0.9916	0.0009	79.5615	6.0241	0.9916	0.0009	79.5615	6.0241	0.9916	0.0009	79.5615	6.0241

Sr. No	Wavelet	R^2	RMSE	SNR	Tmax (hr)	R^2	RMSE	SNR	Tmax (hr)	R^2	RMSE	SNR	Tmax (hr)
		Soft				Hard				Garrote			
28	coif14	0.9916	0.0009	79.5659	6.0241	0.9916	0.0009	79.5659	6.0241	0.9916	0.0009	79.5659	6.0241
29	coif15	0.9916	0.0009	79.5696	6.0241	0.9916	0.0009	79.5696	6.0241	0.9916	0.0009	79.5696	6.0241
30	coif16	0.9916	0.0009	79.5717	6.0241	0.9916	0.0009	79.5717	6.0241	0.9916	0.0009	79.5717	6.0241
31	coif17	0.9916	0.0009	79.5734	6.0241	0.9916	0.0009	79.5734	6.0241	0.9916	0.0009	79.5734	6.0241
32	db1	0.7018	0.0100	30.7204	250.0000	0.7002	0.0100	30.8285	250.0000	0.7019	0.0100	30.7528	250.0000
33	db2	0.9971	0.0021	61.6139	23.8095	0.9980	0.0019	64.1837	23.8095	0.9980	0.0020	62.6082	23.8095
34	db3	0.9996	0.0019	64.2457	23.8095	0.9995	0.0019	64.3833	23.8095	0.9996	0.0019	64.3134	23.8095
35	db4	0.9996	0.0019	64.3086	23.8095	0.9996	0.0019	64.3220	23.8095	0.9996	0.0019	64.3217	23.8095
36	db5	0.9995	0.0019	64.2869	23.8095	0.9995	0.0018	64.7453	23.8095	0.9995	0.0019	64.2999	23.8095
37	db6	0.9996	0.0019	64.3101	23.8095	0.9996	0.0019	64.3101	23.8095	0.9996	0.0019	64.3101	23.8095
38	db7	0.9997	0.0019	64.4370	23.8095	0.9997	0.0019	64.4370	23.8095	0.9997	0.0019	64.4370	23.8095
39	db8	0.9994	0.0019	64.3585	23.8095	0.9994	0.0019	64.3585	23.8095	0.9994	0.0019	64.3585	23.8095
40	db9	0.9996	0.0018	64.5580	23.8095	0.9994	0.0018	64.6454	23.8095	0.9996	0.0018	64.5800	23.8095
41	db10	0.9996	0.0018	64.8289	23.8095	0.9996	0.0018	64.8289	23.8095	0.9996	0.0018	64.8289	23.8095
42	db11	0.9992	0.0018	64.8963	23.8095	0.9991	0.0018	64.9812	23.8095	0.9992	0.0018	64.9080	23.8095
43	db12	0.9996	0.0018	64.4971	23.8095	0.9996	0.0018	64.4971	23.8095	0.9996	0.0018	64.4971	23.8095
44	db13	0.9994	0.0018	64.9032	23.8095	0.9994	0.0018	64.9032	23.8095	0.9994	0.0018	64.9032	23.8095
45	db14	0.9993	0.0018	64.7269	23.8095	0.9993	0.0018	64.7269	23.8095	0.9993	0.0018	64.7269	23.8095
46	db15	0.9996	0.0018	64.5790	23.8095	0.9996	0.0018	64.5577	23.8095	0.9996	0.0018	64.5794	23.8095
47	db16	0.9996	0.0018	64.7662	23.8095	0.9995	0.0018	64.8414	23.8095	0.9996	0.0018	64.7775	23.8095
48	db17	0.9932	0.0011	74.2461	11.9048	0.9931	0.0011	74.4690	11.9048	0.9932	0.0011	74.2934	11.9048
49	db18	0.9934	0.0012	73.7823	11.9048	0.9933	0.0012	73.9724	11.9048	0.9934	0.0012	73.8021	11.9048
50	db19	0.9933	0.0011	74.0246	11.9048	0.9933	0.0011	74.0246	11.9048	0.9933	0.0011	74.0246	11.9048
51	db20	0.9934	0.0012	73.9549	11.9048	0.9934	0.0012	73.9549	11.9048	0.9934	0.0012	73.9549	11.9048
52	db21	0.9933	0.0012	73.8642	11.9048	0.9933	0.0012	73.8642	11.9048	0.9933	0.0012	73.8642	11.9048
53	db22	0.9933	0.0011	74.0639	11.9048	0.9933	0.0011	74.0639	11.9048	0.9933	0.0011	74.0639	11.9048
54	db23	0.9933	0.0012	73.7999	11.9048	0.9933	0.0012	73.7999	11.9048	0.9933	0.0012	73.7999	11.9048
55	db24	0.9933	0.0011	74.0893	11.9048	0.9933	0.0011	74.0893	11.9048	0.9933	0.0011	74.0893	11.9048
56	db25	0.9933	0.0012	73.9528	11.9048	0.9932	0.0011	74.1590	11.9048	0.9933	0.0011	74.0308	11.9048
57	db26	0.9933	0.0011	74.0774	11.9048	0.9932	0.0011	74.3077	11.9048	0.9933	0.0011	74.1074	11.9048
58	db27	0.9933	0.0012	73.8408	11.9048	0.9933	0.0012	73.8408	11.9048	0.9933	0.0012	73.8408	11.9048
59	db28	0.9933	0.0011	74.0139	11.9048	0.9933	0.0011	74.0139	11.9048	0.9933	0.0011	74.0139	11.9048
60	db29	0.9933	0.0012	73.8608	11.9048	0.9933	0.0012	73.8608	11.9048	0.9933	0.0012	73.8608	11.9048
61	db30	0.9933	0.0012	73.9737	11.9048	0.9933	0.0012	73.9737	11.9048	0.9933	0.0012	73.9737	11.9048
62	db31	0.9933	0.0012	73.9632	11.9048	0.9932	0.0011	74.1540	11.9048	0.9933	0.0012	73.9969	11.9048
63	db32	0.9916	0.0009	79.5172	6.0241	0.9916	0.0009	79.5172	6.0241	0.9916	0.0009	79.5172	6.0241
64	db33	0.9916	0.0009	79.7047	6.0241	0.9915	0.0008	80.1107	6.0241	0.9916	0.0009	79.7815	6.0241
65	db34	0.9916	0.0009	79.7282	6.0241	0.9915	0.0008	80.1142	6.0241	0.9916	0.0009	79.8527	6.0241
66	db35	0.9916	0.0009	79.5155	6.0241	0.9915	0.0009	79.8725	6.0241	0.9916	0.0009	79.5214	6.0241
67	db36	0.9916	0.0009	79.5951	6.0241	0.9916	0.0009	79.5951	6.0241	0.9916	0.0009	79.5951	6.0241
68	db37	0.9916	0.0009	79.5718	6.0241	0.9916	0.0009	79.8670	6.0241	0.9916	0.0009	79.5756	6.0241
69	db38	0.9916	0.0009	79.5220	6.0241	0.9915	0.0009	79.8058	6.0241	0.9916	0.0009	79.5305	6.0241
70	dmey	0.9932	0.0012	73.8915	11.9048	0.9932	0.0012	73.8915	11.9048	0.9932	0.0012	73.8915	11.9048
71	haar	0.7018	0.0100	30.7204	250.0000	0.7002	0.0100	30.8285	250.0000	0.7019	0.0100	30.7528	250.0000
72	rbio1.1	0.7018	0.0100	30.7204	250.0000	0.7002	0.0100	30.8285	250.0000	0.7019	0.0100	30.7528	250.0000
73	rbio1.3	0.9988	0.0019	63.7902	23.8095	0.9988	0.0019	63.7902	23.8095	0.9988	0.0019	63.7902	23.8095
74	rbio1.5	0.9993	0.0019	64.2883	23.8095	0.9993	0.0018	64.5275	23.8095	0.9994	0.0019	64.3886	23.8095
75	rbio2.2	0.9983	0.0020	63.0584	23.8095	0.9984	0.0019	64.3807	23.8095	0.9987	0.0019	63.7072	23.8095
76	rbio2.4	0.9997	0.0019	64.3400	23.8095	0.9997	0.0019	64.3400	23.8095	0.9997	0.0019	64.3400	23.8095
77	rbio2.6	0.9997	0.0019	64.3939	23.8095	0.9987	0.0018	64.6861	23.8095	0.9997	0.0019	64.3952	23.8095
78	rbio2.8	0.9994	0.0018	65.3151	23.8095	0.9960	0.0016	67.2124	23.8095	0.9992	0.0017	65.8330	23.8095
79	rbio3.1	0.0035	0.1808	−27.1492	6.0976	0.0035	0.1801	−27.0730	6.0976	0.0035	0.1807	−27.1478	6.0976
79	rbio3.1	0.0035	0.1808	−27.1492		0.0035	0.1801	−27.0730		0.0035	0.1807	−27.1478	
80	rbio3.3	0.9959	0.0021	61.7791	23.8095	0.9983	0.0020	63.3273	23.8095	0.9972	0.0020	62.5664	23.8095

Sr. No	Wavelet	R^2	RMSE	SNR	Tmax (hr)	R^2	RMSE	SNR	Tmax (hr)	R^2	RMSE	SNR	Tmax (hr)
		Soft				Hard				Garrote			
81	rbio3.5	0.9995	0.0019	64.4754	23.8095	0.9991	0.0018	64.8630	23.8095	0.9995	0.0018	64.6940	23.8095
82	rbio3.7	0.9993	0.0018	65.0757	23.8095	0.9949	0.0019	64.2033	23.8095	0.9990	0.0018	65.3482	23.8095
83	rbio3.9	0.9992	0.0018	65.2380	23.8095	0.9990	0.0018	65.2912	23.8095	0.9992	0.0018	65.2558	23.8095
84	rbio4.4	0.9997	0.0019	64.3445	23.8095	0.9997	0.0019	64.3445	23.8095	0.9997	0.0019	64.3445	23.8095
85	rbio5.5	0.9997	0.0018	64.8369	23.8095	0.9978	0.0017	66.4643	23.8095	0.9996	0.0018	65.1973	23.8095
86	rbio6.8	0.9996	0.0018	65.2262	23.8095	0.9965	0.0016	67.7550	23.8095	0.9995	0.0017	65.7192	23.8095
87	sym2	0.9971	0.0021	61.6139	23.8095	0.9980	0.0019	64.1837	23.8095	0.9980	0.0020	62.6082	23.8095
88	sym3	0.9996	0.0019	64.2457	23.8095	0.9995	0.0019	64.3833	23.8095	0.9996	0.0019	64.3134	23.8095
89	sym4	0.9996	0.0019	64.2514	23.8095	0.9996	0.0019	64.2510	23.8095	0.9996	0.0019	64.2512	23.8095
90	sym5	0.9996	0.0018	64.6842	23.8095	0.9993	0.0018	64.9188	23.8095	0.9995	0.0018	64.8281	23.8095
91	sym6	0.9997	0.0019	64.4227	23.8095	0.9997	0.0019	64.4227	23.8095	0.9997	0.0019	64.4227	23.8095
92	sym7	0.9997	0.0018	64.6437	23.8095	0.9996	0.0018	64.7232	23.8095	0.9997	0.0018	64.7034	23.8095
93	sym8	0.9997	0.0019	64.4406	23.8095	0.9997	0.0019	64.4406	23.8095	0.9997	0.0019	64.4406	23.8095
94	sym9	0.9993	0.0018	64.8065	23.8095	0.9991	0.0018	65.0325	23.8095	0.9993	0.0018	64.8144	23.8095
95	sym10	0.9997	0.0018	64.6212	23.8095	0.9995	0.0018	64.8129	23.8095	0.9997	0.0018	64.6302	23.8095
96	sym11	0.9993	0.0018	64.8497	23.8095	0.9990	0.0018	65.1384	23.8095	0.9993	0.0018	64.8922	23.8095
97	sym12	0.9996	0.0018	64.7768	23.8095	0.9995	0.0018	64.8629	23.8095	0.9996	0.0018	64.7975	23.8095
98	sym13	0.9995	0.0018	64.6509	23.8095	0.9995	0.0018	64.6509	23.8095	0.9995	0.0018	64.6509	23.8095
99	sym14	0.9995	0.0018	64.8144	23.8095	0.9992	0.0018	65.0858	23.8095	0.9995	0.0018	64.8235	23.8095
100	sym15	0.9994	0.0017	65.8801	23.8095	0.9963	0.0015	68.4950	23.8095	0.9991	0.0017	66.7495	23.8095
101	sym16	0.9994	0.0018	65.5488	23.8095	0.9969	0.0016	67.9149	23.8095	0.9993	0.0017	66.0835	23.8095
102	sym17	0.9933	0.0011	74.0730	11.9048	0.9933	0.0011	74.0730	11.9048	0.9933	0.0011	74.0730	11.9048
103	sym18	0.9933	0.0011	74.0696	11.9048	0.9933	0.0011	74.0696	11.9048	0.9933	0.0011	74.0696	11.9048
104	sym19	0.9935	0.0012	73.5325	11.9048	0.9935	0.0012	73.5325	11.9048	0.9935	0.0012	73.5325	11.9048
105	sym20	0.9932	0.0011	74.3336	11.9048	0.9931	0.0011	74.5644	11.9048	0.9932	0.0011	74.3974	11.9048

Wavelet performance matrices for the real-world streamflow signal.

Sr. No	wavelet	R^2	RMSE	SNR	Tmax (hr)	R^2	RMSE	SNR	Tmax (hr)	R^2	RMSE	SNR	Tmax (hr)
		Soft				Hard				Garrote			
0	bior1.1	0.0032	22.1649	15.8243	380.0000	0.0032	22.1649	15.8243	380.0000	0.0030	21.5580	16.3796	380.0000
1	bior1.3	0.0075	3.8402	50.8838	152.0000	0.0075	3.8402	50.8838	152.0000	0.0293	2.3924	60.3481	63.3333
2	bior1.5	0.0230	2.0603	63.3370	31.6667	0.0230	2.0603	63.3370	31.6667	0.0396	1.4126	70.8859	31.6667
3	bior2.2	0.0656	1.5626	68.8679	380.0000	0.0656	1.5626	68.8679	380.0000	0.2025	0.9047	79.7977	23.7500
4	bior2.4	0.0854	1.0757	76.3345	23.7500	0.0854	1.0757	76.3345	23.7500	0.2328	0.6939	85.1016	23.7500
5	bior2.6	0.1162	1.0448	76.9183	23.7500	0.1162	1.0448	76.9183	23.7500	0.2958	0.6619	86.0471	23.7500
6	bior2.8	0.1402	0.9086	79.7118	23.7500	0.1402	0.9086	79.7118	23.7500	0.2976	0.6214	87.3088	23.7500
7	bior3.1	0.0021	4.5923	47.3070	253.3333	0.0021	4.5923	47.3070	253.3333	0.0120	2.9686	56.0330	253.3333
8	bior3.3	0.0261	1.7631	66.4533	126.6667	0.0261	1.7631	66.4533	126.6667	0.0719	1.3378	71.9733	152.0000
9	bior3.5	0.0422	1.3621	71.6136	126.6667	0.0422	1.3621	71.6136	126.6667	0.1056	0.9699	78.4050	126.6667
10	bior3.7	0.1992	0.8526	80.9838	23.7500	0.1992	0.8526	80.9838	23.7500	0.3268	0.6314	86.9908	23.7500
11	bior3.9	0.1232	0.9295	79.2564	23.7500	0.1232	0.9295	79.2564	23.7500	0.2993	0.5889	88.3855	23.7500
12	bior4.4	0.0737	1.1380	75.2097	23.7500	0.0737	1.1380	75.2097	23.7500	0.2598	0.6857	85.3409	23.7500
13	bior5.5	0.0400	1.2702	73.0108	23.7500	0.0400	1.2702	73.0108	23.7500	0.1763	0.7592	83.3045	23.7500
14	bior6.8	0.1647	0.7821	82.7100	23.7500	0.1647	0.7821	82.7100	23.7500	0.3477	0.5002	91.6488	23.7500
15	coif1	0.0196	2.6040	58.6537	253.3333	0.0196	2.6040	58.6537	253.3333	0.0419	1.6314	68.0055	126.6667
16	coif2	0.1086	1.0795	76.2648	23.7500	0.1086	1.0795	76.2648	23.7500	0.2838	0.6668	85.9001	23.7500
17	coif3	0.0781	1.1138	75.6396	23.7500	0.0781	1.1138	75.6396	23.7500	0.2719	0.6377	86.7919	23.7500
18	coif4	0.0330	1.2938	72.6425	23.7500	0.0330	1.2938	72.6425	23.7500	0.1044	0.8393	81.2974	23.7500
19	coif5	0.0673	1.0923	76.0291	25.3333	0.0673	1.0923	76.0291	25.3333	0.3026	0.7041	84.8118	23.7500
20	coif6	0.1536	0.9221	79.4169	23.7500	0.1536	0.9221	79.4169	23.7500	0.3450	0.5754	88.8493	23.7500
21	coif7	0.1048	0.8649	80.6980	23.7500	0.1048	0.8649	80.6980	23.7500	0.3162	0.5482	89.8169	23.7500
22	coif8	0.1166	0.7698	83.0274	23.7500	0.1166	0.7698	83.0274	23.7500	0.3396	0.5023	91.5672	23.7500
23	coif9	0.0037	0.3821	97.0335	12.0635	0.0037	0.3821	97.0335	12.0635	0.0002	0.2388	106.4398	12.0635
24	coif10	0.0037	0.3490	98.8469	12.0635	0.0037	0.3490	98.8469	12.0635	0.0003	0.2337	106.8658	12.0635
25	coif11	0.0026	0.3554	98.4844	12.0635	0.0026	0.3554	98.4844	12.0635	0.0000	0.2303	107.1651	12.0635

Sr. No	wavelet	R^2	RMSE	SNR	Tmax (hr)	R^2	RMSE	SNR	Tmax (hr)	R^2	RMSE	SNR	Tmax (hr)
		Soft				Hard				Garrote			
26	coif12	0.0032	0.3322	99.8357	12.0635	0.0032	0.3322	99.8357	12.0635	0.0006	0.2255	107.5819	12.0635
27	coif13	0.0021	0.3241	100.3305	12.0635	0.0021	0.3241	100.3305	12.0635	0.0002	0.2124	108.7820	12.0635
28	coif14	0.0030	0.3347	99.6862	12.0635	0.0030	0.3347	99.6862	12.0635	0.0005	0.2253	107.6030	12.0635
29	coif15	0.0021	0.3074	101.3853	12.0635	0.0021	0.3074	101.3853	12.0635	0.0003	0.2011	109.8744	12.0635
30	coif16	0.0027	0.3357	99.6263	12.0635	0.0027	0.3357	99.6263	12.0635	0.0003	0.2220	107.8989	12.0635
31	coif17	0.0004	0.1696	113.2769	6.9725	0.0004	0.1696	113.2769	6.9725	0.0001	0.1221	119.8562	5.9843
32	db1	0.0032	22.1649	15.8243	380.0000	0.0032	22.1649	15.8243	380.0000	0.0030	21.5580	16.3796	380.0000
33	db2	0.0006	3.7285	51.4745	253.3333	0.0006	3.7285	51.4745	253.3333	0.0193	2.2519	61.5589	126.6667
34	db3	0.0349	1.4305	70.6339	253.3333	0.0349	1.4305	70.6339	253.3333	0.1335	0.8606	80.7970	23.7500
35	db4	0.0885	1.1122	75.6670	23.7500	0.0885	1.1122	75.6670	23.7500	0.3388	0.6292	87.0598	23.7500
36	db5	0.0804	1.0926	76.0237	23.7500	0.0804	1.0926	76.0237	23.7500	0.2890	0.6063	87.8024	23.7500
37	db6	0.0420	0.9557	78.7010	23.0303	0.0420	0.9557	78.7010	23.0303	0.2114	0.6001	88.0088	23.7500
38	db7	0.0581	1.1198	75.5317	23.7500	0.0581	1.1198	75.5317	23.7500	0.1999	0.6310	87.0021	23.7500
39	db8	0.0295	1.2629	73.1262	28.1481	0.0295	1.2629	73.1262	28.1481	0.1307	0.7647	83.1595	23.7500
40	db9	0.0375	1.3672	71.5394	30.4000	0.0375	1.3672	71.5394	30.4000	0.2444	0.7377	83.8780	23.7500
41	db10	0.0421	1.3667	71.5466	23.7500	0.0421	1.3667	71.5466	23.7500	0.1751	0.7726	82.9556	23.7500
42	db11	0.0108	1.3287	72.1106	17.2727	0.0108	1.3287	72.1106	17.2727	0.0803	0.7489	83.5772	23.7500
43	db12	0.0467	1.2853	72.7751	29.2308	0.0467	1.2853	72.7751	29.2308	0.2183	0.7102	84.6376	23.7500
44	db13	0.0699	0.9980	77.8337	23.7500	0.0699	0.9980	77.8337	23.7500	0.2387	0.5522	89.6731	23.7500
45	db14	0.0128	1.0628	76.5762	29.2308	0.0128	1.0628	76.5762	29.2308	0.0922	0.6510	86.3809	24.5161
46	db15	0.0621	1.0676	76.4861	23.7500	0.0621	1.0676	76.4861	23.7500	0.2182	0.6060	87.8127	23.7500
47	db16	0.0489	0.9404	79.0233	28.1481	0.0489	0.9404	79.0233	28.1481	0.1975	0.5047	91.4686	23.7500
48	db17	0.0169	1.0985	75.9160	29.2308	0.0169	1.0985	75.9160	29.2308	0.1196	0.5629	89.2863	23.7500
49	db18	0.0416	1.1570	74.8770	23.7500	0.0416	1.1570	74.8770	23.7500	0.1448	0.6890	85.2461	23.7500
50	db19	0.0423	1.0317	77.1695	28.1481	0.0423	1.0317	77.1695	28.1481	0.1846	0.5442	89.9649	23.7500
51	db20	0.0040	1.1816	74.4572	29.2308	0.0040	1.1816	74.4572	29.2308	0.0784	0.6055	87.8287	24.5161
52	db21	0.0521	1.0163	77.4715	23.7500	0.0521	1.0163	77.4715	23.7500	0.1691	0.6115	87.6307	23.7500
53	db22	0.0207	1.1247	75.4445	28.1481	0.0207	1.1247	75.4445	28.1481	0.1150	0.6092	87.7068	23.7500
54	db23	0.0136	1.1411	75.1545	29.2308	0.0136	1.1411	75.1545	29.2308	0.0960	0.6104	87.6675	23.7500
55	db24	0.0257	1.0762	76.3261	23.0303	0.0257	1.0762	76.3261	23.0303	0.1876	0.5996	88.0255	23.7500
56	db25	0.0013	0.4015	96.0432	14.9020	0.0013	0.4015	96.0432	14.9020	0.0001	0.2150	108.5366	12.0635
57	db26	0.0028	0.4311	94.6242	13.8182	0.0028	0.4311	94.6242	13.8182	0.0014	0.2458	105.8583	11.8750
58	db27	0.0018	0.4191	95.1865	12.0635	0.0018	0.4191	95.1865	12.0635	0.0004	0.2143	108.6045	11.8750
59	db28	0.0014	0.3925	96.4999	14.9020	0.0014	0.3925	96.4999	14.9020	0.0005	0.2253	107.5997	12.0635
60	db29	0.0014	0.4239	94.9610	12.0635	0.0014	0.4239	94.9610	12.0635	0.0000	0.2160	108.4398	12.0635
61	db30	0.0014	0.3888	96.6891	14.9020	0.0014	0.3888	96.6891	14.9020	0.0003	0.2002	109.9597	12.0635
62	db31	0.0037	0.4131	95.4763	12.0635	0.0037	0.4131	95.4763	12.0635	0.0000	0.2162	108.4283	12.0635
63	db32	0.0022	0.3920	96.5225	14.9020	0.0022	0.3920	96.5225	14.9020	0.0002	0.2000	109.9835	12.0635
64	db33	0.0014	0.4195	95.1693	12.0635	0.0014	0.4195	95.1693	12.0635	0.0000	0.2271	107.4395	12.0635
65	db34	0.0017	0.4054	95.8541	14.9020	0.0017	0.4054	95.8541	14.9020	0.0004	0.2074	109.2575	12.0635
66	db35	0.0014	0.4163	95.3197	14.0741	0.0014	0.4163	95.3197	14.0741	0.0002	0.2442	105.9893	12.0635
67	db36	0.0030	0.3956	96.3415	14.9020	0.0030	0.3956	96.3415	14.9020	0.0000	0.1956	110.4231	12.0635
68	db37	0.0038	0.4013	96.0552	13.8182	0.0038	0.4013	96.0552	13.8182	0.0001	0.2270	107.4514	11.8750
69	db38	0.0044	0.3784	97.2296	14.9020	0.0044	0.3784	97.2296	14.9020	0.0001	0.2005	109.9354	11.8750
70	dmey	0.0036	0.4066	95.7915	12.0635	0.0036	0.4066	95.7915	12.0635	0.0017	0.3066	101.4413	11.8750
71	haar	0.0032	22.1649	15.8243	380.0000	0.0032	22.1649	15.8243	380.0000	0.0030	21.5580	16.3796	380.0000
72	rbio1.1	0.0032	22.1649	15.8243	380.0000	0.0032	22.1649	15.8243	380.0000	0.0030	21.5580	16.3796	380.0000
73	rbio1.3	0.0001	3.3218	53.7845	190.0000	0.0001	3.3218	53.7845	190.0000	0.0128	1.8423	65.5741	190.0000
74	rbio1.5	0.0564	1.4273	70.6782	23.7500	0.0564	1.4273	70.6782	23.7500	0.2034	0.7990	82.2814	23.7500
75	rbio2.2	0.0132	3.3726	53.4806	126.6667	0.0132	3.3726	53.4806	126.6667	0.0155	2.2328	61.7295	126.6667
76	rbio2.4	0.0593	1.0686	76.4673	23.7500	0.0593	1.0686	76.4673	23.7500	0.1502	0.6994	84.9459	23.7500
77	rbio2.6	0.1391	1.0433	76.9466	23.7500	0.1391	1.0433	76.9466	23.7500	0.3254	0.6776	85.5779	23.7500
78	rbio2.8	0.1549	0.8466	81.1244	23.7500	0.1549	0.8466	81.1244	23.7500	0.3451	0.5275	90.5851	23.7500
79	rbio3.1	0.0001	210.9408	−29.2371	6.0800	0.0001	210.9408	−29.2371	6.0800	0.0000	196.6824	−27.8373	6.0800

Sr. No	wavelet	R^2	RMSE	SNR	Tmax (hr)	R^2	RMSE	SNR	Tmax (hr)	R^2	RMSE	SNR	Tmax (hr)
		Soft				Hard				Garrote			
80	rbio3.3	0.0344	2.0937	63.0155	23.7500	0.0344	2.0937	63.0155	23.7500	0.0723	1.1474	75.0454	23.7500
81	rbio3.5	0.0702	1.6404	67.8957	23.7500	0.0702	1.6404	67.8957	23.7500	0.1340	1.0807	76.2416	23.7500
82	rbio3.7	0.0592	1.3170	72.2873	23.7500	0.0592	1.3170	72.2873	23.7500	0.1333	0.8716	80.5425	23.7500
83	rbio3.9	0.0425	1.0290	77.2230	23.0303	0.0425	1.0290	77.2230	23.0303	0.1504	0.6792	85.5325	23.7500
84	rbio4.4	0.0388	1.2379	73.5265	84.4444	0.0388	1.2379	73.5265	84.4444	0.1448	0.7714	82.9866	23.7500
85	rbio5.5	0.0455	1.1860	74.3834	23.7500	0.0455	1.1860	74.3834	23.7500	0.2193	0.7072	84.7240	23.7500
86	rbio6.8	0.1084	1.1402	75.1702	23.7500	0.1084	1.1402	75.1702	23.7500	0.2919	0.6881	85.2702	23.7500
87	sym2	0.0006	3.7285	51.4745	253.3333	0.0006	3.7285	51.4745	253.3333	0.0193	2.2519	61.5589	126.6667
88	sym3	0.0349	1.4305	70.6339	253.3333	0.0349	1.4305	70.6339	253.3333	0.1335	0.8606	80.7970	23.7500
89	sym4	0.0451	1.2663	73.0729	23.7500	0.0451	1.2663	73.0729	23.7500	0.2168	0.7548	83.4197	23.7500
90	sym5	0.0849	1.2062	74.0455	23.7500	0.0849	1.2062	74.0455	23.7500	0.2377	0.7785	82.8032	23.7500
91	sym6	0.0162	1.6055	68.3260	84.4444	0.0162	1.6055	68.3260	84.4444	0.1138	0.9514	78.7908	23.7500
92	sym7	0.0859	1.0644	76.5462	23.7500	0.0859	1.0644	76.5462	23.7500	0.2588	0.6312	86.9974	23.7500
93	sym8	0.1259	1.0906	76.0594	23.7500	0.1259	1.0906	76.0594	23.7500	0.3022	0.6640	85.9845	23.7500
94	sym9	0.0553	1.0953	75.9746	25.3333	0.0553	1.0953	75.9746	25.3333	0.2550	0.6271	87.1290	23.7500
95	sym10	0.1274	0.8280	81.5696	23.7500	0.1274	0.8280	81.5696	23.7500	0.3099	0.5036	91.5138	23.7500
96	sym11	0.0693	1.0877	76.1133	23.7500	0.0693	1.0877	76.1133	23.7500	0.3020	0.6440	86.5943	23.7500
97	sym12	0.1090	1.1156	75.6058	23.7500	0.1090	1.1156	75.6058	23.7500	0.3202	0.6801	85.5060	23.7500
98	sym13	0.0875	1.1402	75.1699	25.3333	0.0875	1.1402	75.1699	25.3333	0.3174	0.6375	86.7982	23.7500
99	sym14	0.0638	1.2850	72.7796	23.7500	0.0638	1.2850	72.7796	23.7500	0.2479	0.7327	84.0155	23.7500
100	sym15	0.0457	1.3243	72.1764	25.3333	0.0457	1.3243	72.1764	25.3333	0.2205	0.7385	83.8581	23.7500
101	sym16	0.0684	1.1971	74.1957	23.7500	0.0684	1.1971	74.1957	23.7500	0.3063	0.7036	84.8256	23.7500
102	sym17	0.0313	1.5879	68.5460	22.3529	0.0313	1.5879	68.5460	22.3529	0.0758	1.0004	77.7875	22.3529
103	sym18	0.0169	1.3158	72.3053	29.2308	0.0169	1.3158	72.3053	29.2308	0.1092	0.8013	82.2247	23.7500
104	sym19	0.1790	0.7877	82.5669	23.7500	0.1790	0.7877	82.5669	23.7500	0.3387	0.5007	91.6307	23.7500
105	sym20	0.1093	0.9113	79.6523	23.7500	0.1093	0.9113	79.6523	23.7500	0.3507	0.5713	88.9916	23.7500

Author contributions M.W.S.: Conceptualization, Methodology, Formal analysis, Investigation, Validation, Visualization, A.S.: Conceptualization, Resources, Supervision, Writing—Review and Editing, Visualization.

Funding Open Access funding enabled and organized by CAUL and its Member Institutions
The authors declare that no funds, grants, or other support were received during the preparation of this manuscript.

Data availability No datasets were generated or analysed during the current study.

Declarations

Conflict of interest The authors declare no competing interests.

Ethical approval The authors confirm that the publication does not need ethical approval.

Consent to participate This study did not require informed consent from participants as it did not include human data and only utilised publicly available geological data.

Consent to publish No consent to publish was necessary as the data used is already in the public domain and does not contain any identifiable personal information.

References

Adamowski J, Sun K (2010) Development of a coupled wavelet transform and neural network method for flow forecasting of non-perennial rivers in semi-arid watersheds. J Hydrol 390(1–2):85–91. https://doi.org/10.1016/j.jhydrol.2010.06.033

Addison PS (2018) Introduction to redundancy rules: The continuous wavelet transform comes of age. Philos Trans R Soc a Math Phys Eng Sci 376(2126):20170258. https://doi.org/10.1098/rsta.2017.0258

Anbalagan T, Nath MK, Vijayalakshmi D, Anbalagan A (2023) Analysis of various techniques for ECG signal in healthcare, past, present, and future. Biomed Eng Adv 6:100089. https://doi.org/10.1016/j.bea.2023.100089

Barnard HR, Graham CB, Van Verseveld WJ, Brooks JR, Bond BJ, McDonnell JJ (2010) Mechanistic assessment of hillslope transpiration controls of diel subsurface flow: a steady-state irrigation

approach. Ecohydrology 3:133–142. https://doi.org/10.1002/eco.114
Boronina A, Golubev S, Balderer W (2005) Estimation of actual evapotranspiration from an alluvial aquifer of the Kouris catchment (Cyprus) using continuous streamflow records. Hydrol Process 19(20):4055–4068. https://doi.org/10.1002/hyp.5871
Briciu A-E, Graur A, Oprea DI, Filote C (2019) A methodology for the fast comparison of streamwater diurnal cycles at two monitoring points. Water 11(12):2524. https://doi.org/10.3390/w11122524
Cadol D, Kampf S, Wohl E (2012) Effects of evapotranspiration on baseflow in a tropical headwater catchment. J Hydrol 462–463:4–14. https://doi.org/10.1016/j.jhydrol.2012.04.060
Chong KL, Lai SH, El-Shafie A (2019) Wavelet transform based method for river stream flow time series frequency analysis and assessment in tropical environment. Water Resour Manage 33(6):2015–2032. https://doi.org/10.1007/s11269-019-02226-7
Czikowsky MJ, Fitzjarrald DR (2004) Evidence of seasonal changes in evapotranspiration in eastern U.S. hydrological records. J Hydrometeorol 5(5):974–988. https://doi.org/10.1175/1525-7541(2004)005%3c0974:EOSCIE%3e2.0.CO;2
Daubechies I (1988) Orthonormal bases of compactly supported wavelets. Commun Pure Appl Math 41(7):909–996. https://doi.org/10.1002/cpa.3160410705
Debnath L, Shah FA (2017) Lecture notes on wavelet transforms. Springer. https://doi.org/10.1007/978-3-319-59433-0
Flinchem EP, Jay DA (2000) An introduction to wavelet transform tidal analysis methods. Estuar Coast Shelf Sci 51(2):177–200. https://doi.org/10.1006/ecss.2000.0586
Fourati W, Kammoun F, Bouhlel MS (2005) Medical image denoising using wavelet thresholding. J Test Eval 33(5):364–369. https://doi.org/10.1520/JTE12481
Gao H-Y (1998) Wavelet shrinkage denoising using the non-negative garrote. J Comput Graph Stat 7(4):469–488. https://doi.org/10.1080/10618600.1998.10474789
Graham CB, Barnard HR, Kavanagh KL, McNamara JP (2012) Catchment scale controls the temporal connection of transpiration and diel fluctuations in streamflow. Hydrol Process 27(18):2541–2556
Gribovszki Z, Kalicz P, Kucsara M, Szilágyi J, Vig P (2008) Evapotranspiration calculation on the basis of the riparian zone water balance. Acta Silvatica et Lignaria Hungarica.
Grinsted A, Moore JC, Jevrejeva S (2004) Application of the cross wavelet transform and wavelet coherence to geophysical time series. Nonlinear Processes Geophys 11(5/6):561–566
Huang J, Cao L, Yu F, Liu X, Wang L (2021) Groundwater drought and cycles in Xuchang City, China. Front Earth Sci 9:736305. https://doi.org/10.3389/feart.2021.736305
Inouye T, Harper T, Rasmussen NC (1969) Application of fourier transforms to the analysis of spectral data. Nucl Inst Methods 67(1):125–132. https://doi.org/10.1016/0029-554X(69)90551-5
Johnstone IM, Silverman BW (1997) Wavelet threshold estimators for data with correlated noise. J R Stat Soc Ser B (Methodological) 59(2):319–351
Kirchner JW, Godsey SE, Solomon M, Osterhuber R, McConnell JR, Penna D (2020) The pulse of a montane ecosystem: coupling between daily cycles in solar flux, snowmelt, transpiration, groundwater, and streamflow at Sagehen Creek and Independence Creek, Sierra Nevada, USA. Hydrol Earth Syst Sci 24(11):5095–5123. https://doi.org/10.5194/hess-24-5095-2020
Locci-Lopez D, Zhang R, Oyem A, Castagna J (2018) The multiscale Fourier transform. SEG Techn Progr Expanded Abstr 2018:4176–4180. https://doi.org/10.1190/segam2018-2994723.1
Loheide SP II (2008) A method for estimating subdaily evapotranspiration of shallow groundwater using diurnal water table fluctuations. Ecohydrology 1(1):59–66. https://doi.org/10.1002/eco.7
Lukas V, Novák J, Neudert L, Svobodova I, Rodriguez-Moreno F, Edrees M, Kren J (2016) The combination of UAV survey and Landsat imagery for monitoring of crop vigor in precision agriculture. Int Arch Photogr Remote Sens Spat Inf Sci ISPRS Arch 41(July):953–957. https://doi.org/10.5194/isprsarchives-XLI-B8-953-2016
Lundquist JD, Cayan DR (2002) Seasonal and spatial patterns in diurnal cycles in streamflow in the western United States. J Hydrometeorol 3(5):591–603. https://doi.org/10.1175/1525-7541(2002)003%3c0591:saspid%3e2.0.co;2
Mallat S (2009) A wavelet tour of signal processing. Elsevier. https://doi.org/10.1016/B978-0-12-374370-1.X0001-8
Misiti M, Misiti Y, Oppenheim G, Jean-Michel Poggi (eds) (2007) Wavelets and their applications. Wiley, Denver. https://doi.org/10.1002/9780470612491
Percival DB (2008) Analysis of geophysical time series using discrete wavelet transforms: an overview. In: Donner RV, Barbosa SM (eds) Nonlinear time series analysis in the geosciences: applications in climatology, geodynamics and solar-terrestrial physics. Springer, Berlin, pp 61–79. https://doi.org/10.1007/978-3-540-78938-3_4
Rhif M, Ben Abbes A, Farah IR, Martínez B, Sang Y (2019) Wavelet transform application for/in non-stationary time-series analysis: a review. Appl Sci 9(7):7. https://doi.org/10.3390/app9071345
Sang Y-F (2012) A practical guide to discrete wavelet decomposition of hydrologic time series. Water Resour Manage 26(11):3345–3365. https://doi.org/10.1007/s11269-012-0075-4
Sang Y-F (2013) A review on the applications of wavelet transform in hydrology time series analysis. Atmos Res 122:8–15. https://doi.org/10.1016/j.atmosres.2012.11.003
Santos CAG, de Morais BS (2013) Identification of precipitation zones within São Francisco River basin (Brazil) by global wavelet power spectra. Hydrol Sci J 58(4):789–796. https://doi.org/10.1080/02626667.2013.778412
Sarwar MW, Campbell DI, Shokri A (2022) Riparian zone as a variable source area for the estimation of evapotranspiration through the analysis of daily fluctuations in streamflow. Hydrol Process 36(10):e14708. https://doi.org/10.1002/hyp.14708
Satchithanantham S, Wilson HF, Glenn AJ (2017) Contrasting patterns of groundwater evapotranspiration in grass and tree dominated riparian zones of a temperate agricultural catchment. J Hydrol. https://doi.org/10.1016/j.jhydrol.2017.04.016
Smith LC, Turcotte DL, Isacks BL (1998) Stream flow characterization and feature detection using a discrete wavelet transform. Hydrol Process 12(2):233–249. https://doi.org/10.1002/(SICI)1099-1085(199802)12:2%3c233::AID-HYP573%3e3.0.CO;2-3
Széles B, Broer M, Parajka J, Hogan P, Eder A, Strauss P, Blöschl G (2018) Separation of scales in transpiration effects on low flows: a spatial analysis in the hydrological open air laboratory. Water Resour Res 54(9):6168–6188. https://doi.org/10.1029/2017WR022037
Torrence C, Compo GP (1998) A practical guide to wavelet analysis. Bull Am Meteor Soc 79(1):61–78. https://doi.org/10.1175/1520-0477(1998)079%3c0061:APGTWA%3e2.0.CO;2
Troxell HC (1936) The diurnal fluctuation in the ground-water and flow of the santa ana river and its meaning. Trans Am Geophys Union 17(2):496. https://doi.org/10.1029/TR017i002p00496
Tschinkel HM (1963) Short-term fluctuation in streamflow as related to evaporation and transpiration. J Geophys Res 68(24):6459–6469. https://doi.org/10.1029/JZ068i024p06459
Vetterli M, Herley C (1992) Wavelets and filter banks: theory and design. IEEE Trans Signal Process 40(9):2207–2232. https://doi.org/10.1109/78.157221
White WN (1932) A method of estimating ground-water supplies based on discharge by plants and evaporation from soil: results of investigations in Escalante Valley, Utah. In Water supply paper: Vol. A (Issue 659). US Geological Survey. https://doi.org/10.3133/wsp659A

Wilcock RJ, Betteridge K, Shearman D, Fowles CR, Scarsbrook MR, Thorrold BS, Costall D (2009) Riparian protection and on-farm best management practices for restoration of a lowland stream in an intensive dairy farming catchment: a case study. NZ J Mar Freshwat Res 43(3):803–818. https://doi.org/10.1080/00288330909510042

Wu X, Zhou J, Yu H, Liu D, Xie K, Chen Y, Hu J, Sun H, Xing F (2021) The development of a hybrid wavelet-ARIMA-LSTM model for precipitation amounts and drought analysis. Atmosphere 12(1):1. https://doi.org/10.3390/atmos12010074

Xiao C, Yuan W, Yu R (2018) Diurnal cycle of rainfall in amount, frequency, intensity, duration, and the seasonality over the UK. Int J Climatol 38(13):4967–4978. https://doi.org/10.1002/joc.5790

Yan J, Laflamme S, Singh P, Sadhu A, Dodson J (2020) A comparison of time-frequency methods for real-time application to high-rate dynamic systems. Vibration 3(3):3. https://doi.org/10.3390/vibration3030016

Yang Z, Kallergi M, DeVore RA, Lucier BJ, Qian W, Clark RA, Clarke LP (1995) Effect of wavelet bases on compressing digital mammograms. IEEE Eng Med Biol Mag 14(5):570–577. https://doi.org/10.1109/51.464773

Zhang A, Zheng C, Wang S, Yao Y (2015) Analysis of streamflow variations in the Heihe River Basin, Northwest China: trends, abrupt changes, driving factors and ecological influences. J Hydrol Reg Stud 3:106–124. https://doi.org/10.1016/j.ejrh.2014.10.005